

IDEA League

MASTER OF SCIENCE IN APPLIED GEOPHYSICS
RESEARCH THESIS

Quantifying Uncertainty in Fractured Geothermal Reservoirs Using a Discrete Fracture Model

Ariel T. Thomas

August 19, 2016

Quantifying Uncertainty in Fractured Geothermal Reservoirs Using a Discrete Fracture Model

MASTER OF SCIENCE THESIS

for the degree of Master of Science in Applied Geophysics at
Delft University of Technology

ETH Zürich

RWTH Aachen University

by

Ariel T. Thomas

August 19, 2016

Department of Geoscience & Engineering	·	Delft University of Technology
Department of Earth Sciences	·	ETH Zürich
Faculty of Georesources and Material Engineering	·	RWTH Aachen University



Delft University of Technology

Copyright © 2013 by IDEA League Joint Master's in Applied Geophysics:

Delft University of Technology, ETH Zürich, RWTH Aachen University

All rights reserved.

No part of the material protected by this copyright notice may be reproduced or utilized in any form or by any means, electronic or mechanical, including photocopying or by any information storage and retrieval system, without permission from this publisher.

Printed in The Netherlands, Switzerland, Germany

IDEA LEAGUE
JOINT MASTER'S IN APPLIED GEOPHYSICS

Delft University of Technology, The Netherlands
ETH Zürich, Switzerland
RWTH Aachen, Germany

Dated: *August 19, 2016*

Supervisor(s):

Prof. Dr. Christoph Clauser

Johanna Bruckmann

Tao Chen

Committee Members:

Prof. Dr. Christoph Clauser

Johanna Bruckmann

Tao Chen

Prof. Dr. Hansruedi Maurer

Eidesstattliche Versicherung

Thomas, Ariel

Name, Vorname

352232

Matrikelnummer (freiwillige Angabe)

Ich versichere hiermit an Eides Statt, dass ich die vorliegende Arbeit/Bachelorarbeit/
Masterarbeit* mit dem Titel

Quantifying Uncertainty in Fractured Geothermal Reservoirs Using
a Discrete Fracture Model

selbständig und ohne unzulässige fremde Hilfe erbracht habe. Ich habe keine anderen als die angegebenen Quellen und Hilfsmittel benutzt. Für den Fall, dass die Arbeit zusätzlich auf einem Datenträger eingereicht wird, erkläre ich, dass die schriftliche und die elektronische Form vollständig übereinstimmen. Die Arbeit hat in gleicher oder ähnlicher Form noch keiner Prüfungsbehörde vorgelegen.

Aachen, 12-08-2016

Ort, Datum



Unterschrift

*Nichtzutreffendes bitte streichen

Belehrung:

§ 156 StGB: Falsche Versicherung an Eides Statt

Wer vor einer zur Abnahme einer Versicherung an Eides Statt zuständigen Behörde eine solche Versicherung falsch abgibt oder unter Berufung auf eine solche Versicherung falsch aussagt, wird mit Freiheitsstrafe bis zu drei Jahren oder mit Geldstrafe bestraft.

§ 161 StGB: Fahrlässiger Falscheid; fahrlässige falsche Versicherung an Eides Statt

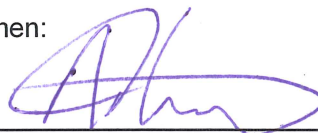
(1) Wenn eine der in den §§ 154 bis 156 bezeichneten Handlungen aus Fahrlässigkeit begangen worden ist, so tritt Freiheitsstrafe bis zu einem Jahr oder Geldstrafe ein.

(2) Straflosigkeit tritt ein, wenn der Täter die falsche Angabe rechtzeitig berichtigt. Die Vorschriften des § 158 Abs. 2 und 3 gelten entsprechend.

Die vorstehende Belehrung habe ich zur Kenntnis genommen:

Aachen, 12-08-2016

Ort, Datum



Unterschrift

Abstract

Fractures occur at varying scales and orientations in the subsurface. The role of fractures as conduits for fluid flow in a reservoir must be well constrained for planning and development of a geothermal system. This study examines the uncertainty associated with fractures in a rock matrix using a discrete fracture network modelling approach; fractures are considered as discrete elements embedded in a rock matrix. Many fractures are below the resolution of geophysical investigation methods and are therefore typically described by a statistical distribution of permeability, length and orientation. A Monte Carlo approach is used whereby multiple reservoir simulations are conducted using fracture network parameters drawn randomly from a pre-defined distribution. The simulation results show that fracture permeability is the major factor which influences the production. An increase in fracture network permeability from $8.33 \times 10^{-12} \text{ m}^2$ to $8.33 \times 10^{-10} \text{ m}^2$ showed an increase of uncertainty in reservoir production by up to a factor of six when considering the standard deviation. The results show that this uncertainty increases by up to 200 % with the life of the reservoir for the high permeability case. Stochastic analysis of the azimuth uncertainty revealed an opposite trend where a decrease in uncertainty of 34 % was observed over the 30 year simulated lifetime of the reservoir. The orientation of fractures in the reservoir was found to play an important role in the temperature field in the reservoir with increases in production temperature ranging from 0.5 K to 3 K resulting from the proximity of fractures to the production well. The results also indicate that discrete fracture networks which possess similar orientations of fractures produce statistically similar production profiles. The findings of this study show that a stochastic approach can be used for efficient planning of geothermal doublet systems based on expected trends in production.

Acknowledgements

First of all I want to thank my supervisors, Tao Chen and Johanna Bruckmann for their constructive feedback throughout the duration of this project. Their guidance enabled me to overcome several challenges along the way. I would also like to thank Prof. Dr. Christoph Clauser for his counsel in setting the project on the right track from an early stage.

I thank my colleague Nicolas Boehm for the stimulating discussions, for the long nights we were working together before deadline, and all the fun we had along the way.

Last but not the least, I would like to thank my family: my parents and my Congress WBN family for supporting me spiritually throughout writing this thesis and my life in general.

RWTH Aachen University
August 19, 2016

Ariel T. Thomas

Table of Contents

Abstract	vii
Acknowledgements	ix
Acronyms	xix
1 Introduction	1
1 Theory and Modelling Techniques	3
2 Theory	5
2-1 Geothermal Doublet Systems	5
2-2 Representative Elementary Volume	6
2-3 Subsurface Heat Flow and Transport	6
2-4 Fluid Flow in Fractured Porous Media	8
2-5 Discrete Fracture Network Modelling	10
3 Modelling Techniques	13
3-1 Reservoir and Simulation Parameters	13
3-2 Finite Element Meshing	15
3-2-1 Part 1: GMSH	16
3-2-2 Part 2: HyperMesh/TetGen	17
3-3 Discrete Fracture Network Models	17
3-4 Stochastic Analysis	19
3-4-1 Quantitative Analysis Approach	20

II	Results and Analysis	23
4	Observations	25
4-1	Part I	25
4-1-1	Base Case I	25
4-1-2	Permeability Study I	26
4-1-3	Permeability Experiment	28
4-2	Azimuth Experiment	29
4-3	Part II	30
4-3-1	Base Case II	30
4-4	Azimuth Study	31
4-5	Permeability Study II	32
4-5-1	Fracture Geometry and Temperature Distribution	36
	Dynamics of the Cold Water Front	37
5	Quantitative Analysis	39
5-1	Geometry I Model	39
5-1-1	Permeability Uncertainty Analysis	39
	Comparing Decline Rates	40
	Skewness	41
5-1-2	Azimuth Uncertainty Analysis	42
5-2	Geometry II Model	44
5-2-1	Permeability Uncertainty Analysis	44
	Skewness	45
5-2-2	Comparing the Discrete Fracture Networks	46
	Fracture Geometry and Temperature Distribution	47
6	Discussion	49
7	Conclusion	51
	Bibliography	53
A	Supplementary Images and Plots	57
A-1	Pumping Rate Test	57
A-2	Azimuth Study	58
A-3	Single Fracture Permeability Experiment - Geometry II	59
A-3-1	Low Permeability	59
A-3-2	High Permeability	60

B	Data Files and Formats	61
B-1	OpenGeoSys File Format	61
B-1-1	Input File Examples	61
	Geometry File - .gli	61
	Boundary Condition File - .bc	62
	Initial Condition File- .ic	63
	Source Term File - .st	63
	Fluid Properties File - .mfp	63
	Solid Properties File - .msp	63
	Medium Properties File - .mmp	64
	Numerical Settings Parameter File - .num	64
	Time Stepping File - .tim	65
	Output Settings File - .out	65
	Process Settings File - .pcs	65
B-2	GMSH Files	66
C	Programming	67
C-1	Python	67
C-1-1	Python: Conversion of Petrel DFN for HyperMesh	67
C-1-2	Python: Generating multiple input files	69
C-2	Matlab	70
C-2-1	Matlab: Generation of random fracture parameters	70
C-2-2	Matlab: Generation of Histogram Plots	71

List of Figures

3-1	Reservoir geometries showing the simplified case of a single embedded fracture connecting injection(blue) and production(red) wells	14
3-2	Simplified example of two intersecting planar features showing mesh refinement at the intersection. - not drawn to scale	16
3-3	Mesh generated using GMSH. The embedded fracture consists of triangular elements (orange) and the matrix tetrahedral elements (green)	16
3-4	Two stages (a and b) of the meshing process for the DFN model.The complexity of the mesh can be appreciated by the cluster of tetrahedral elements around intricate fracture geometries	17
3-5	DFN-1: Orthogonal (a) and map view (b) of manually created DFN geometry. The network contains eight fractures of varying orientations and also intersections.	18
3-6	Petrel™ Generated DFN	19
3-7	Schematic representation of fracture azimuth considered in this study. Red and blue arrow represents the injection and production well - not drawn to scale	20
3-8	Probability Distributions generated using Matlab	20
4-1	Matrix only base case showing reservoir temperature distribution after 30 years in map view and cross-section view	25
4-2	Temperature production profile for matrix only base case in Geometry II	26
4-3	Comparison of production temperature profile for a varying values of permeability	26
4-4	Map view of reservoir with single embedded fracture showing the contrast between low and high permeability. The snapshots at 15 and 30 years show that the heat transfer is confined to a smaller region around fractures when the permeability is higher	27
4-5	Production Temperature Profile of low (a) and high (b) permeability scenarios. The grey lines represent the distribution of 200 realisations. The contrast between the distributions shows the weight of the influence is dependent on the ratio of permeability between the fracture and the surrounding matrix. Average response is plotted in red.	28

4-6	Plot of 100 temperature production profiles for azimuth uncertainty analysis, mean production profile shown in red and the matrix case shown in blue. Symmetrical distribution of profiles about the mean and variations in initial ($t = 0$) temperature distribution can be observed.	30
4-7	Matrix only base case showing reservoir temperature distribution after 30 years in map view(a) and cross-section view (b)	31
4-8	Temperature production profile for matrix only base case in Geometry II	31
4-9	Comparison of temperature production profile for azimuth values from $0^\circ - 60^\circ$	32
4-10	Production Temperature Profile of low (l) and high (r) permeability scenarios. The grey lines represent the distribution of 100 realisations. Average response is plotted in red.	33
4-11	Comparison of flow paths for DFN-1 (left) and single fracture (right). Depth slices at 1900m	34
4-12	Contrast of the uncertainty associated with permeability in two different discrete fracture network models.	35
4-13	Temperature production profiles showing the influence of increasing number of fractures in the reservoir	36
4-14	DFN-1 (1st row), DFN-2(2nd row), DFN-3(3rd row) Comparison of progression of cold water front in reservoir - Map View @ $z = 1900$ m	38
4-15	DFN-1 (1st row), DFN-2(2nd row), DFN-3(3rd row) Comparison of progression of cold water front in reservoir - Cross Section View	38
5-1	Production Temperature Profile of low (a) and high (b) permeability scenarios. The percentiles shown in green (80th) and magenta (20th) lines indicate the spread of the distribution which can be seen to increase with time.	40
5-2	Percentage Decline plot of low (a) and high (b) permeability scenarios including the matrix decline rate (blue) for comparison. The average trend is plotted as a bold red line. It can be seen that the reservoir heat is depleted at a different rate in the cases where a fracture is present	41
5-3	Distribution of production profiles for high permeability fracture scenario at 5, 15 and 30 years.	42
5-4	(a) Experiment results including mean trend in red and standard deviation as dashed magenta lines. The distribution is symmetric about the mean (b) Normalised percentage decline	43
5-5	Production Temperature Profile of low (a) and high (b) permeability scenarios. Data shows greater contrast between the distributions in the low and high permeability scenarios when a DFN is involved as opposed to a single embedded fracture.	44
5-6	Normalised decline plots showing comparison of results from three fracture networks and the matrix case.	47
A-1	Temperature production profile for varying pumping rates while holding all other parameters constant. Increased pumping rate corresponding to increased temperature drawdown and earlier thermal breakthrough	57
A-2	Meshes used for Azimuth study: (a) 10° (b) 20° (c) 30° (d) 40° (e) 50° (f) 60°	58
A-3	Production Temperature Profile for high permeability single fracture embedded in geometry II	59
A-4	Production Temperature Profile for high permeability single fracture embedded in geometry II	60

List of Tables

3-1	Rock Properties of Simulated Reservoir Matrix	14
3-2	Fluid Properties of Injected Water	14
3-3	Simulation Parameters	15
5-1	Summary of temperature percentiles for Low Permeability	39
5-2	Summary of temperature percentiles for High Permeability	40
5-3	Statistic Summary: low permeability single embedded fracture	42
5-4	Statistic Summary: high permeability single embedded fracture	42
5-5	Statistical summary of Azimuth uncertainty analysis over the life of the reservoir	43
5-6	Summary of production temperature percentiles for DFN-1 with low permeability	45
5-7	Summary of production temperature percentiles for DFN-1 with high permeability	45
5-8	Statistic Summary: DFN-1 with low permeability	45
5-9	Statistic Summary: DFN-1 with high permeability	45
5-10	Statistic Summary: DFN-2	46
5-11	Statistic Summary: DFN-3	46
5-12	Summary of normalised percentage decline for three discrete fracture networks and matrix case	47
A-1	Summary of statistics for single fracture embedded in geometry II with low	59
A-2	Summary of statistics for single high permeability fracture embedded in geometry II	60
B-1	Required Input Files	61

Acronyms

DUT Delft University of Technology
ETH Swiss Federal Institute of Technology
RWTH Aachen University
DFN Discrete Fracture Network
REV Representative Elementary Volume
EGS Enhanced Geothermal System
OGS OpenGeoSys

Chapter 1

Introduction

Geothermal energy is a clean and renewable energy source which utilizes the heat contained in rocks and fluids within rock pores and fractures in the Earth's crust. There are several external as well as internal sources that contribute to the Earth's thermal budget. Among the most significant of these are solar irradiation, original heat and radiogenic heat derived from the decay of unstable, radioactive isotopes. Geothermal energy has a wide range of applications from direct uses such as building heating or green houses to flash steam generation to produce clean electricity. A key component affecting the productivity of Geothermal reservoir is rock hydraulic conductivity which is controlled by porosity, permeability and specifically the fracture distribution in the reservoir.

Fractures are an ubiquitous part of geological systems and have a considerable impact on flow paths and rates within geothermal reservoirs. Therefore, they have a direct impact on the productivity and efficiency of the system and should be taken into consideration. Direct and detailed measurement of fractures within a reservoir is not feasible on a reservoir scale. Most fractures are also below seismic resolution. Therefore, several approaches have been considered toward establishing a fracture network model. The study of fractures and flow in geothermal reservoirs has taken two major paths, a simplified view of a discrete fracture network or an approximation by upscaling fractures to an equivalent porous medium. This approach was used in [Blum et al. \(2009\)](#), where block scale equivalent hydraulic properties were modeled after a Discrete Fracture Network (DFN) described by power law statistics for fracture length and distribution. An empirical Barton-Bandis model was used to simulate the Hydro-Mechanical behavior of the fractures. It was found that the assumptions made in building a continuum model may result in a limited range of variability in simulated hydrological and mechanical properties. The incorporation of lateral heterogeneity in formation properties is essential to improving continuum model performance.

Alternative approaches use sampled particle velocities of DFN simulations and fitted these velocities to probability distributions which were subsequently used in Monte Carlo simulations ([Schwartz and Smith 1988](#)). One disadvantage of equivalent medium models is that they do not contain explicit information about fracture length, orientation and distribution. [Berkowitz et al. \(2000\)](#) showed that the percolation threshold, or the point above which a

fracture network is considered as well connected, is affected at certain scales by the minimum fracture length in the system. Another approach is a Dual continuum method, whereby the fracture and matrix system are treated as separate but overlapping continua which are coupled through matrix-fracture transfer function (Hao et al. 2013). In this study, upscaling was achieved by directly mapping discrete fractures onto continuum grid blocks and calculating an effective permeability tensor.

The generation of a discrete fracture networks can be achieved by utilizing both deterministic or stochastic methods. In the scope of this project a stochastic approach will be taken toward generating a DFN in a hypothetical geothermal reservoir. This requires statistical descriptions of fracture parameters. The greatest challenge to this approach in many cases has been obtaining reliable statistics from limited subsurface data. One novel approach for overcoming this problem is explained in Dorn et al. (2013), where hydraulic, tracer and GPR reflection data are used to condition connected 3D DFN models.

In this study, both the fracture network and rock matrix will be considered. A simple model consisting of a block representation of a reservoir unit will be generated using PetrelTM, a geological modelling software by Schlumberger. The discrete fracture modeling module will be used to generate the fractures which will then be exported as geometrical objects. A finite element mesh will then be generated for numerical simulation. The increased complexity of the fracture network translates to a more complicated meshing problem. As a consequence, the study will be conducted with two reservoir geometries. An open source three-dimensional finite element mesh generator called Gmsh (Geuzaine and Remacle 2009), will be used to generate a mesh of for the geometry I; a simplified single fracture case. A combination of HyperMesh (Hyperworks 2009), a more robust feature based finite element modeling software, and TetGen (Si 2007) will be used for geometry II; PetrelTM generated DFNs. Finally, OpenGeoSys will be used for the simulation. This is an open source finite element simulator for solving thermal, hydraulic, mechanical and chemical processes in fractured media (Kolditz et al. 2012). The result of the reservoir simulations include temperate distribution in the reservoir throughout the lifetime as well as the production temperature curve. A Monte Carlo approach will be used for uncertainty analysis. Various distributions of fracture network parameters such as aperture and azimuth will be generated and a number of deterministic simulations run using random values from these distributions. The results of these simulations will then be aggregated and a statistical analysis performed to ascertain how the uncertainty associated with characteristics of the fracture network such as permeability, azimuth and fracture length distribution may affect the reservoir production.

Part I

Theory and Modelling Techniques

Chapter 2

Theory

2-1 Geothermal Doublet Systems

The heat content of a hydrothermal aquifer can be utilized by producing the hot fluid and by subsequently re-injecting the waste cooled water into the aquifer. This scheme is known as a doublet system as was first introduced by [Gringarten and Sauty \(1975\)](#). The produced fluid is replaced, often at the same rate, by cool injected water. After a period known as the thermal breakthrough time, the temperature of the produced fluid decreases. The lifetime of a reservoir depends on how it is developed ([Gringarten 1979](#)); factors such as the pumping rate and the offset distance between injection and production wells. However, a shut-in of the field can allow the natural energy flow to slowly replenish the geothermal system as described by [Satman \(2011\)](#), thus making such doublet systems renewable and sustainable.

The heat content of the fluid forms the basis for categorisation of geothermal systems as either high or low enthalpy. High enthalpy systems can produce electricity directly from hot steam or from a high-temperature two-phase fluid. Low-enthalpy systems use the warm or hot water directly or via a heat exchanger for localised or district heating. High enthalpy systems are consistent with extreme geothermal gradients and very high ground temperatures at relatively shallow depths, typically associated with volcanically active regions. Low-enthalpy systems on the other hand can be deployed in any region with average to slightly elevated geothermal gradients. Hydrothermal systems are typically connected to aquifers and are produced at a rate which corresponds to the installed capacity of their heating or power plant facilities.

Rocks at depth are permeable due to fractures and pore spaces between mineral grains. The injected water is heated via contact with the rock and returns to the surface through producing wells. The heat transfer in the medium takes places mainly through conduction and convection and these processes are further discussed in a following section. In some cases, efficiently producing a geothermal system requires improving the natural permeability of the rock. Stimulating a fracture system is usually achieved by hydraulic fracturing, and such a geothermal reservoir is termed as Engineered or Enhanced Geothermal System (EGS) ([McLarty and Grabowski 1998](#)). Hereby, the rock is stimulated to improve permeability by creating

new fractures, opening existing fractures or dissolving the rock. Injection and production wells are placed such that they intersect as many permeable fractures as possible. The cool injected water moves through preferential pathways in the reservoir via the fracture network. Due to the key role that permeability plays in the system efficiency, it is very important to characterize the fracture network to properly understand the system.

2-2 Representative Elementary Volume

The Representative Elementary Volume (**REV**) is an important principle when describing hydrogeological and thermal properties in a reservoir. It is a volume of a property field which is large enough to be structurally entirely typical of the whole mixture on average. Also referred to as the unit cell, it represents the smallest volume over which measurement can be made which will yield a value representative of the whole. These properties can include any averaged quantities used to characterize physical systems such as a reservoir. Consider measuring samples of a porous medium to determine effective thermal conductivity, λ_{eff} , if the sample size is too small, readings will tend to oscillate. As the sample size increases, the readings subsequently become more consistent. A satisfactory condition for the **REV** is when measured properties fluctuate about a mean with a wavelength which is small relative to the dimensions of the sample and the effects of this fluctuation become insignificant within a few wavelengths from the surface (Hill 1963). The reliability of defining a **REV** for a fractured rock mass is an issue of concern due to the fact that fluid flow in fractured rock has been shown to be strongly scale-dependent. The inherent high level of complexity and heterogeneity in a fracture system weakens the guarantee that a **REV** can be determined for a particular rock mass (Long et al. 1982; Neuman 1988). The **DFN** approach of this study eliminates the need for consideration of a **REV** where fracture properties (hydraulic conductivity) are concerned, since the fractures are discretely represented in the rock matrix.

2-3 Subsurface Heat Flow and Transport

Heat conduction through fully saturated matrices is dependent on the matrix structure and the thermal conductivity of each phase. In this study, it is assumed that a single-phase fluid (water) is occupying the pores. Since thermal conductivity varies considerably between the solid and fluid phase within the medium, the manner in which the solid is interconnected significantly influences the heat transport process in a geothermal reservoir. Among the main factors that contribute to the efficiency of a fractured geothermal system are the geometry of rock mass bounded by interconnected fractures and the flow rate and velocity in the fracture network. These factors are all dependent on geometry as well as hydraulic properties of the fracture network. Quantifying the influence of discrete fractures within the matrix can improve understanding of geothermal reservoir performance.

Heat transport in a fractured porous medium can be considered primarily through two processes. Conductive heat transport from rock matrix to fractures containing fluid and advective transport through fracture networks. Additionally, heat dispersion within the solid phase can play a role. However, heat dispersion will not be considered in this study so as to isolate the

influence of the fracture network. The problem is further simplified by neglecting thermal dissipation, generation and radiation effects.

Analysis of the heat flow through heterogeneous media on a macroscopic level is simplified by local spatially-averaged properties over a certain representative elementary volume. Key thermal properties such as effective thermal conductivity $\langle \lambda_{eff} \rangle$ and heat capacity $\langle \rho c_p \rangle$ are derived from the application of first principles to the REV. The local average heat capacity is determined by simple volume averaging, however, the effective thermal conductivity is dependent on the thermal conductivity of each phase in addition to the structure of the solid matrix, i.e. the continuity of the solid phase.

In the context of geothermal energy systems, local thermodynamic equilibrium is assumed. In principle, at the pore level, there will be a difference between the temperature at a point in the solid and the fluid phase ΔT_d . In addition to this, there also exists a maximum temperature difference across the representative elementary volume ΔT_l . However, under the assumption of local thermal equilibrium, these temperature differences are negligible compared to those occurring across the system, ΔT_L . The assumption of local thermal equilibrium is invoked by requiring that

$$\Delta T_d < \Delta T_l \ll \Delta T_L. \quad (2-1)$$

This physically means that the energy exchange between the phases is significantly faster than the energy transport within a phase. Given this negligible local temperature difference between the phases, we assume that within the REV, $V = V_f + V_s$ the solid and fluid phases are in local thermal equilibrium, such that,

$$\frac{1}{V_f} \int_{V_f} T_f dV = \frac{1}{V_s} \int_{V_s} T_s dV = \frac{1}{V} \int_V T dV. \quad (2-2)$$

As a result the most important heat transport processes in porous fractured medium are conduction (solid phase), advection and heat storage.

In this study, the finite element meshing of the reservoir geometry is such that the rock matrix is represented by tetrahedron (3D) elements and fractures by triangular (2D) elements. The fractures are therefore two-dimensional hydraulic conduits in three-dimensional space; it follows that fluid pressure and temperature are assumed to be constant across the fracture width. Additionally, instantaneous flow and heat exchange between medium and fracture network are assumed. The heat transport equation taking into account advective and diffusive fluxes is

$$\overline{\rho c_p} \frac{\delta T}{\delta t} + \rho^l c_p^l v \cdot \Delta T - \Delta(\bar{\lambda} \Delta T) = Q_T, \quad (2-3)$$

where $\overline{\rho c_p} = n \rho^l c_p^l + (1-n) \rho^s c_p^s$ is the heat storage of porous medium with a porosity n , specific heat capacity of fluid c_p^l , fluid density ρ^l , specific heat capacity of rock c_p^s and rock density ρ^s . Q_T is the heat source/sink term, v denotes the Darcy velocity, $\bar{\lambda} = n \lambda^l + (1-n) \lambda^s$ is the effective heat conductivity of porous medium with λ^l fluid and λ^s rock heat conductivity.

2-4 Fluid Flow in Fractured Porous Media

A porous medium consists of different phases, a solid and at least one fluid phase. Fluid flow in porous media is typically approached as a continuum problem as the exact geometry cannot be resolved on a micro scale. According to the REV concept, all the details about the microscopic structure of the medium need not be known, rather, the proportion of each phase can be described macroscopically by porosity and saturation.

The laws governing mass and momentum conservation of fluid phases and their constitutive relations together govern fluid flow in a porous medium. The equations are simplified by a number of assumptions for practical modelling purposes:

- *Fluid phase assumption:* Pore spaces can be filled in theory by two fluid phases, liquid and a gas phase. In this case, the gas phase is assumed to be stagnant. This reduces the problem to a single-phase flow where only the liquid phase is considered as a dynamic phase.
- *Capillary pressure assumption:* Liquid saturation is derived from capillary pressure. Considering that the density of liquid is much higher than gas (e.g., $\rho^{water}/\rho^{air} \approx 800$), it can be concluded that the gravitational effects of the gas pressure are negligible in comparison to liquid pressure. As a result constant gas pressure can be assumed. This simplifies the capillary pressure relation so the liquid phase is then decoupled from the gas phase, allowing the flow and transport process of the liquid phase to be modelled independently.
- *Momentum equation assumption:* It is assumed that the liquid phase moves slowly in the porous medium. Accordingly, the momentum balance for the fluid phase can be described by the Darcy equation

$$\mathbf{q} = -\frac{\boldsymbol{\kappa}}{\mu} \nabla p, \quad (2-4)$$

where $\boldsymbol{\kappa}$ is the fluid independent permeability tensor of the porous medium, ∇p is the pressure gradient tensor, μ is the fluid viscosity. This postulates that the rate of water flow through a medium is proportional to the hydraulic head gradient.

- *Fully Saturated Medium* Considering the medium pores to be completely filled results in further simplification of the momentum balance equations which govern the Darcy-type flow. The time-dependent saturation term is no longer considered (i.e. $\epsilon \frac{\delta s}{\delta t} = 0$).

Further simplification can be achieved by considering the aquifer as a closed system, i.e. by implementing no flow bounding surfaces. Groundwater flow in porous media can thus be derived from the conservation principles of mass and momentum. Firstly, consider the static state equation of fluid mass balance for a porous medium. In this case, flow fluid is only possible in the pore spaces. The pore space is characterized by the medium porosity n . The equation thus follows,

$$\frac{\delta n \rho}{\delta t} + \nabla \cdot (n \rho \mathbf{v}) = Q_f. \quad (2-5)$$

In the case of an incompressible fluid (e.g. water), which is considered as the reservoir fluid in this study, density is no longer time dependent and so equation 2-5 becomes

$$\rho \frac{\delta n}{\delta t} + \rho \nabla \cdot (n\mathbf{v}) = Q_f. \quad (2-6)$$

This condition of incompressibility means that fluid density is nearly constant, $\rho = \rho_0$, dividing by this reference density yields,

$$\frac{\delta n}{\delta t} + \nabla \cdot (n\mathbf{v}) = \frac{Q_f}{\rho_0}. \quad (2-7)$$

There exists a linear relationship between temporal changes in porosity and groundwater pressure shown below in equation 2-8. The factor is given by the storativity coefficient, S , which is a hydrological parameter which defines the volume of water that an aquifer releases from or takes into storage per unit surface area of the aquifer per unit change in head normal to that surface.

$$\frac{\delta n}{\delta t} = S \frac{\delta h}{\delta t}. \quad (2-8)$$

We must now consider Darcy's law which postulates that the rate of flow through a porous medium is proportional to the hydraulic head gradient. Darcy's law follows

$$\mathbf{v} = -\mathbf{K} \nabla h. \quad (2-9)$$

Combining the above mass balance equation (Eq.2-6) and the constitutive relationships in equations 2-8 and 2-9 we obtain finally the groundwater flow equation

$$S \frac{\delta h}{\delta t} + \nabla \cdot (\mathbf{K} \nabla h) = Q_f, \quad (2-10)$$

where:

- h hydraulic head (m)
- n porosity
- \mathbf{K} Hydraulic conductivity tensor (m/s)
- \mathbf{q} Darcy velocity (m/s)
- Q_f source/sink term (kg/m^3s)
- S storage coefficient ($1/m$)
- t time (s)
- ρ fluid density (kg/m^3)
- \mathbf{v} pore velocity (m/s)

The Hydraulic conductivity, \mathbf{K} of a medium is related to the intrinsic permeability, κ as shown in Equation 2-14. Using this relationship as well as the assumption that change in hydraulic head is only due to gravitational acceleration, the equation can be expressed

$$S_s \frac{\delta p}{\delta t} - \nabla \cdot \left(\frac{\kappa}{\mu} (\nabla p + \rho^l \mathbf{g}) \right) = Q_f, \quad (2-11)$$

where $S_s = (\alpha - n)/K_s + n/K_l$ is the specific storage of the medium with α the Biot-Willis coefficient, n porosity, K_s & K_l the solid and liquid compressibility respectively. p is liquid pressure, \mathbf{g} is the gravity acceleration vector and Q_f is the volumetric fluid source/sink term. The Biot-Willis coefficient $\alpha \approx 1$ under the assumption of an isotropic porous medium and incompressible grains. This form of the equation is more intuitive for this study as it directly contains parameters implemented in OpenGeoSys for reservoir simulation.

2-5 Discrete Fracture Network Modelling

Fractures are among the most abundant features found in the subsurface. The economic development of a fractured geothermal reservoir requires a reasonable understanding of the nature of fractures and the structure of their network (fracture length, connectivity, aperture etc.). Most geological formations are highly fractured down to several hundreds of meters below the surface. As a result, the problem of accurately representing fracture spatial distribution has been widely studied and continues to be an active area of research (Berkowitz 2002; Willis et al. 2006). A major constraint is that there is seldom sufficient volume available where fracture parameters can be directly measured. Consequently, many techniques and models have been developed for characterization of fractures and their networks. The characterization of fractured porous media falls into three distinct, but related parts, namely

1. a single fracture
2. a network of fractures
3. a fractured porous medium

Fracture networks generally have a complex organization, long-range spatial correlation and scattered length and aperture distributions. It has been widely found that distribution of fracture lengths in a network vary between power-law and log normal distributions, dependent on the sample size (Nicol et al. 1996) or fracture density (Reches 1986). Considering a discrete network of fractures, let $n_l(\ell)$ be the number density of fractures with lengths in the interval $[\ell, \ell + d\ell]$ given $d\ell \ll \ell$. Then, the power-law distribution of fractures' length is defined by

$$n_l(\ell) = a_l \ell^{-a}, \quad (2-12)$$

where a_l is a constant related to fracture density and a is the characteristic exponent (Sahimi 2011).

Fracture aperture is one of the most important properties which controls its flow and transport properties. In reality, the internal surface of a fracture is rough and therefore there is typically a distribution of the aperture within a given fracture. Aperture is also closely related to

the permeability of a fracture. A cubic law has been adapted as a means of deriving the intrinsic permeability of a fracture from its aperture as discussed in Witherspoon et al. (1980). Assuming fracture faces to be parallel and planar plates, through which laminar flow occurs, studies have shown that the hydraulic conductivity, K_f of a fracture with aperture a , is given by

$$K_f = \frac{a^2 \rho g}{12\mu}, \quad (2-13)$$

where g is gravitational acceleration and μ is the fluid viscosity. Hydraulic conductivity is related to intrinsic permeability by

$$K_f = \frac{\kappa_f^f \rho g}{\mu}. \quad (2-14)$$

Accordingly, a relationship can be obtained between aperture and permeability

$$\kappa_f = \frac{a^2}{12}. \quad (2-15)$$

This relationship is used to determine values of fracture permeability for simulations in this study. The effects of uncertainty at low and high permeability thresholds will be investigated.

Another controlling feature for fracture network permeability is the extent to which fractures are interconnected and form continuous flow pathways. This relationship between fracture interconnectedness and permeability is referred to in literature as Percolation Theory. The interconnection between given fracture sets is a complex function of fracture density and fracture extent or size. Long and Witherspoon (1985) showed that the permeability of the system increases as the fracture length increases and the density is proportionally decreased. It was also found that a system with shorter but more dense fractures behaves less like a porous medium than a system with longer less dense fractures. Intuition would suggest that network permeability may simply be proportional to number of fractures; however, this relationship is complicated by three factors. Considering a discrete network, some fractures may be isolated from the network and therefore not contributing to an actual flow path. Additionally, a discrete fracture that is connected to the network at only one end does not contribute to the overall network permeability. Finally, if a connected fracture is indeed conducting fluid, its contribution may be dependent on the conditions of its connectivity. For example, if it is connected by a fracture with very low permeability then this becomes a controlling factor on the flow in this fracture. In this study, the ratio of fracture length to reservoir volume was considered as a metric for interconnectedness. The effects of varying this parameter was be investigated.

Modelling Techniques

3-1 Reservoir and Simulation Parameters

The reservoir simulation was conducted using OpenGeoSys (OGS). It provides a flexible numerical framework utilizing Finite Element Method for solving multi-field problems in fractured porous media (Kolditz et al. 2012). OGS requires a set of input files which are named according to the specific project and carry file extensions corresponding to the input data type contained within the file. In this study, a naming scheme is used whereby project names are a combination of the prefix 'res' followed by a number which serves as a model identifier. A complete simulation consists of 12 input files, a full list of the file extensions and their meaning can be found in Table B-1. Together, these files fully describe rock and fluid properties as well as simulation parameters such as boundary and initial conditions, source terms and numerical parameters. An example of each of the input files can be seen in the section B-1-1 of the Appendix.

The rock and fluid properties (Tables 3-1 and 3-2) were kept constant across all simulations conducted in this study, in order to isolate the influence of fracture attributes. The study was split into two sections. The first section includes a number of experiments in a simplified single fracture case, with a reservoir dimensions $4 \text{ km} \times 3 \text{ km} \times 0.5 \text{ km}$. The second sections was conducted with reservoir dimensions $2 \text{ km} \times 1 \text{ km} \times 0.5 \text{ km}$. This reduction of the reservoir volume was due to the complexity of the finite element meshing when considering a realistic distribution of discrete fractures. High angle fracture intersections and other complications could not be resolved for a large reservoir. The two reservoir geometries are shown in Figure 3-1.

The rock properties represent a carbonate reservoir with density and heat conductivity values which are typical of a Dolomitic Limestone reservoir (Robertson 1988). The permeability of the rock has been deliberately set to a very low value in an attempt to ensure that effect of the fractures on heat transport processes in the reservoir are maximized. The depth to the top of the reservoir is 1.5 km. This was achieved in simulation by setting a constant pressure boundary condition at the top of the reservoir equivalent to hydrostatic pressure

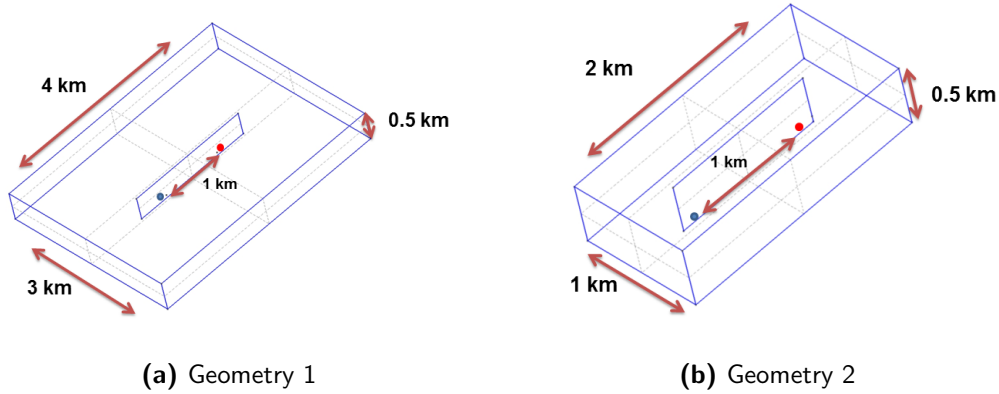


Figure 3-1: Reservoir geometries showing the simplified case of a single embedded fracture connecting injection (blue) and production (red) wells

at 1.5 km depth. The initial pressure distribution in the reservoir was defined according to normal hydrostatic pressure gradient, $P = \rho gh$ (See B-1-1). Injection and production rates were kept constant throughout the simulation and these were defined as equal and opposite flow rates from point sources located 100 m above the base of the reservoir. The full suite of simulation parameters are summarized in Table 3-3.

Table 3-1: Rock Properties of Simulated Reservoir Matrix

Symbol	Property	Value	Unit
n	Porosity	0.014	
κ	Intrinsic Permeability Tensor	9.9×10^{-18}	m^2
S_s	Specific Storage	1.0×10^{-10}	Pa^{-1}
ρ	Density	2763	kg m^{-3}
λ	Heat Conductivity	3.35	$\text{W m}^{-1}\text{K}^{-1}$
α	Thermal Expansion Coefficient	2.4×10^{-5}	K^{-1}

Table 3-2: Fluid Properties of Injected Water

Symbol	Property	Value	Unit
ρ	Density	983 (at 60°C)	kg m^{-3}
μ	Dynamic Viscosity	4.6×10^{-4} (at 60°C)	Pa s
c	Specific Heat Capacity	4186	$\text{J kg}^{-1}\text{K}^{-1}$
λ	Heat Conductivity	0.6	$\text{W m}^{-1}\text{K}^{-1}$

There are a number of assumptions which serve to simplify the problem of simulating groundwater flow in a fractured porous medium. The following assumptions were made:

1. Aquifer is assumed to be horizontal and of uniform thickness
2. The reservoir is a closed system, i.e. no fluid flow or heat exchange occurs at the boundaries.

3. Total injection rate, q is constant and equal to the total production rate.
4. Initial conditions in the reservoir are such that the water and rock matrix are at the same temperature.
5. Properties such as porosity, matrix permeability and thermal conductivity are homogeneously distributed in the reservoir.

Table 3-3: Simulation Parameters

	Parameter	Value	Unit
Source Terms	Injection	0.05	$\text{m}^3 \text{s}^{-1}$
	Production	-0.05	$\text{m}^3 \text{s}^{-1}$
Boundary Condition	Injection Temperature	40	$^{\circ}\text{C}$
	Outer Boundary	No flow and heat exchange	
Initial Conditions	Pressure	14.715	MPa
	Temperature	40	$^{\circ}\text{C}$
	Temperature Gradient	0.022	K m^{-1}
	Hydrostatic Pressure Gradient	9.81×10^3	Pa m^{-1}

3-2 Finite Element Meshing

The finite element mesh is used to subdivide the domain into smaller domain called elements, over which the continuum balance equations are discretely applied. A quality mesh will enable the realistic prediction of reservoir behaviour with high accuracy. The problem of meshing a fractured reservoir requires balancing element size and quality to achieve numerical stability. It is difficult to find optimal settings to satisfy criteria such as the Courant-Friedrichs-Lewy (CFL) condition due to the inhomogeneous fluid velocity which is an inherent part of fluid flow in a fractured medium. The CFL condition is the required condition for solving partial differential equations numerically whereby the time step must be below a threshold to ensure convergence of the solution (Courant et al. 1928). step A maximum element size of 100 m was decided for these simulations. The mesh must also be refined at intersection of fractures where smaller spatial discretisation is needed to better handle the higher fluid velocities. An example of such refinement can be seen in Figure 3-2.

The mesh generation for this study was performed using two different software packages applied based on varying complexity of the reservoir geometry. Performing simulations in OGS requires that the mesh has specific characteristics:

- Fractures are represented by triangular elements.
- Rock Matrix is represented by tetrahedral elements.
- Triangular elements and tetrahedral elements have shared nodes.

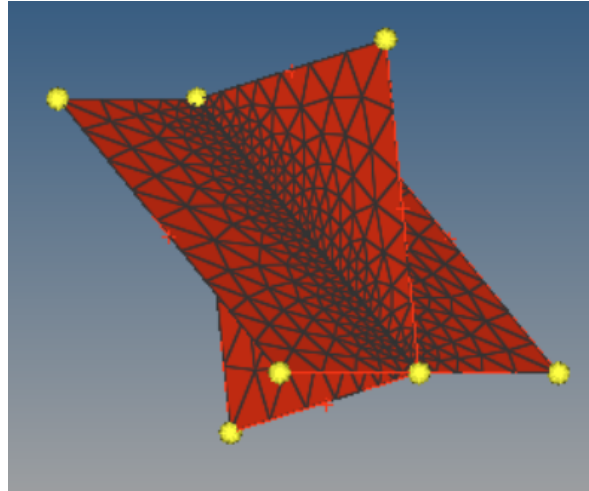


Figure 3-2: Simplified example of two intersecting planar features showing mesh refinement at the intersection. - not drawn to scale

Meeting these criteria is fairly straight forward for the simple reservoir case, where a single fracture embedded in the rock matrix is considered. The meshing of the DFN however produces the problem of intersecting elements at areas of high complexity. Each fracture network requires slightly different meshing parameters such as element size and quality index. A trial and error approach was used as no two sets of fractures could be successfully meshed using the same parameters. Given the available tools, this proved to be a significant limitation to the range of networks that could be simulated.

3-2-1 Part 1: GMSH

GMSH was used to mesh the simplified single fracture case used in the first part of this study. The geometry was constructed in GMSH by defining corner points, connecting lines, surfaces and finally the enclosed volume. An extract of the geometry file can be seen in the Appendix B-2. The finite element mesh of the geometry shown in Figure 3-1b is shown in Figure 3-3.

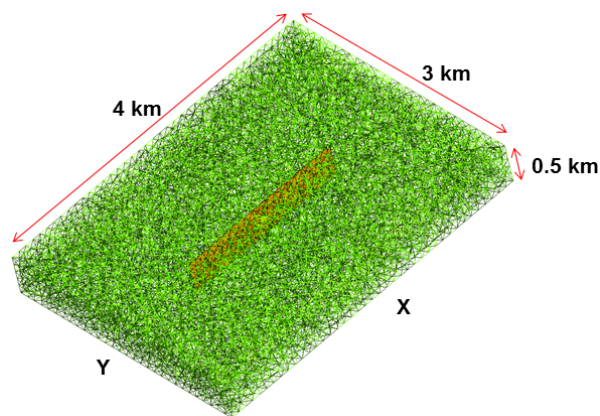


Figure 3-3: Mesh generated using GMSH. The embedded fracture consists of triangular elements (orange) and the matrix tetrahedral elements (green)

3-2-2 Part 2: HyperMesh/TetGen

The more realistic and complex DFN models generated using PetrelTM were meshed using two software packages. The fault geometry first had to be translated from PetrelTM to a format which can be read by HyperMesh. A Python script which can be found in Appendix C-1-1 performs the transformation. The geometry is built up in HyperMesh similarly to GMSH whereby points form the basis of the structure and lines, surfaces and volumes are defined on this framework. HyperMesh is particularly useful for its capability in finding and trimming planes at intersections. This feature was used to handle the complex geometries where several dozens of intersections can occur. The 2D mesh was generated after intersections had been identified, additionally, refinement and quality control of the 2D mesh was performed using built-in tools. The successful 2D mesh was then exported and the tetrahedral elements were generated on this framework using TetGen. Figure 3-4 shows the two stages of the meshing process. The complexity of the final mesh (Fig. 3-4b) can be appreciated when compared to the mesh displayed in Figure 3-3.

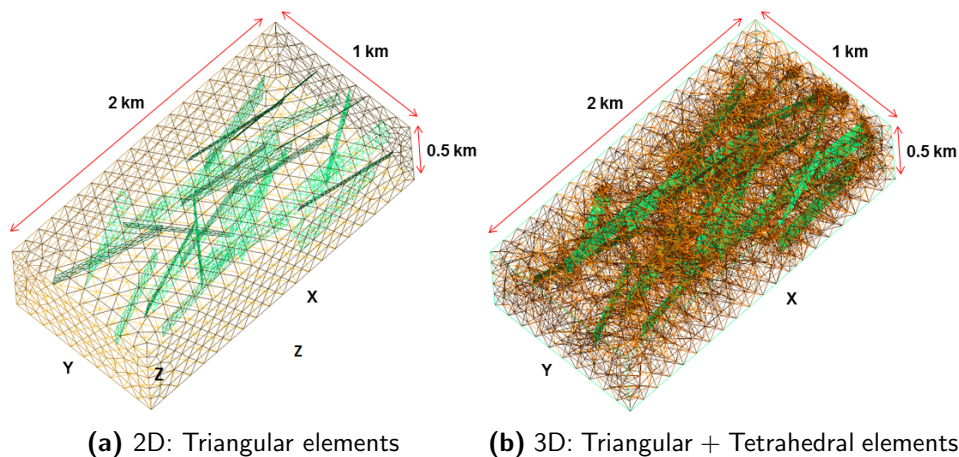


Figure 3-4: Two stages (a and b) of the meshing process for the DFN model. The complexity of the mesh can be appreciated by the cluster of tetrahedral elements around intricate fracture geometries

3-3 Discrete Fracture Network Models

There are three DFN models that were used in this study, the first and most simple was constructed manually using GMSH. This model contains just eight discrete fractures with varying orientations and a few intersections. The model was designed as an intermediate step between the matrix base case and the smallest fracture density that can be successfully generated with PetrelTM. The geometry can be seen in Figure 3-5. It can be seen that the general trend of the network orientation is along strike with the injection/production wells.

The remaining two models were generated using PetrelTM. The models were designed in such a way to satisfy the restrictions of the meshing tools. In this regard, the fracture lengths were relatively long so as to provide conduits throughout the matrix without considerable complexity. Longer fractures minimize the number of intersections that have to be handled

by the meshing algorithm. Petrel™ fracture modelling module offers four categories by which a DFN can be defined. These include Distribution (fracture density), Geometry (shape and length), Orientation and Aperture. The last option is not implemented for this study. A break-down of the parameters follows.

- **Distribution:** Fracture density was defined for both networks using the ratio fracture length/rock volume. A measure referred to as P31 in literature (Dershowitz et al. 1992). The value was set to $3.0 \times 10^{-4} \text{ m}^{-1}$
- **Geometry:** *Shape* - Fractures are conceptually viewed as ellipses but this is computationally expensive so a value of 4 was set to generate only rectangular shaped fractures. Fracture length to height ratio was also set to 4 to generate very elongated features. *Length* - Mean value of 800 m and 600 m for DFN-2 and DFN-3 respectively. The standard deviation in both cases was set to 30.
- **Orientation:** Fisher model was employed which describes a standard distribution of angles whereby the directions to the normal of the fracture plane are scattered around a mean dip and azimuth. The dip and azimuth were set to 90° and 0° respectively for both networks. A concentration factor which is inversely related to the standard deviation was set to a low threshold of 5.

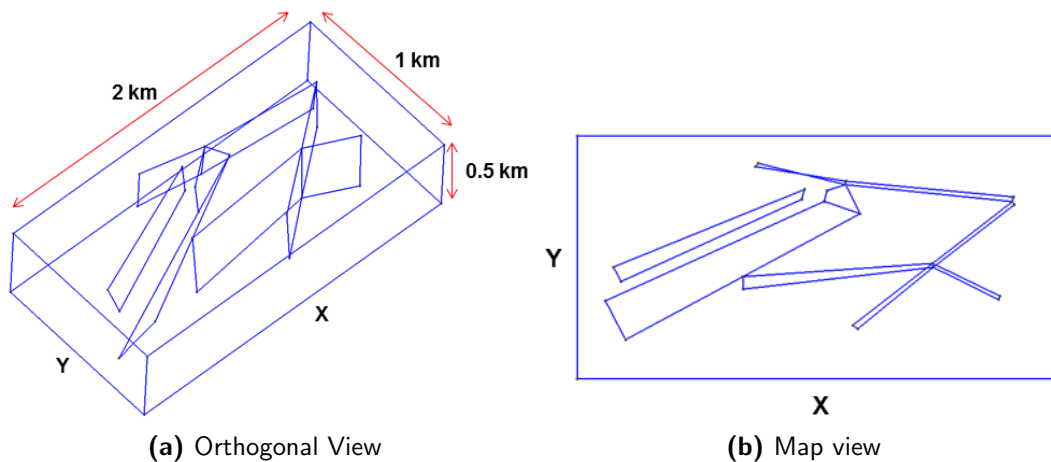
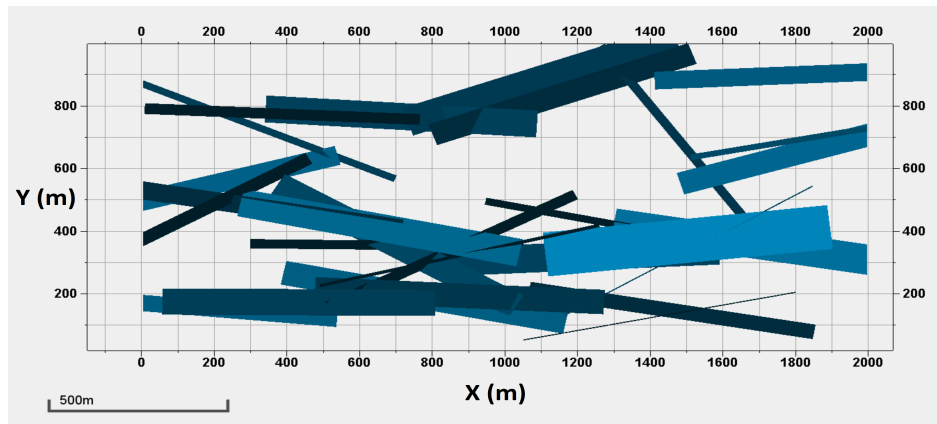
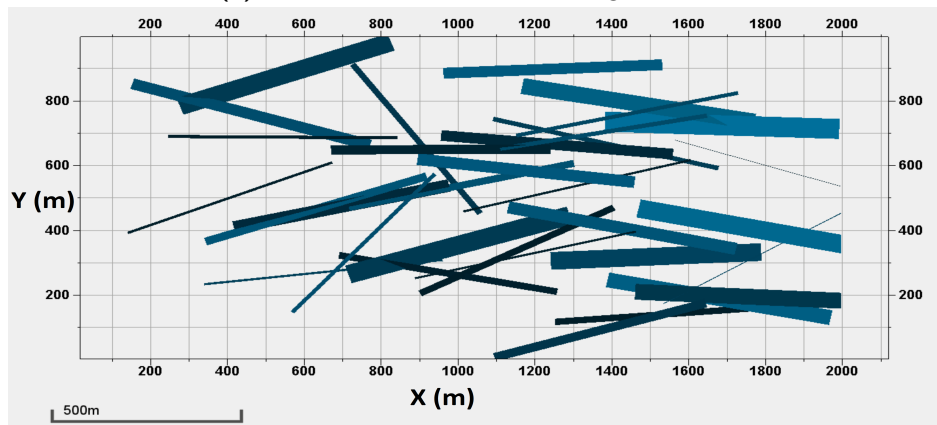


Figure 3-5: DFN-1: Orthogonal (a) and map view (b) of manually created DFN geometry. The network contains eight fractures of varying orientations and also intersections.



(a) DFN 2: 28 fractures, mean length - 800 m



(b) DFN 3: 33 fractures, mean length - 600 m

Figure 3-6: Petrel™ Generated DFN

3-4 Stochastic Analysis

The quantitative analysis of uncertainty was performed using a Monte Carlo approach. The Monte Carlo method is widely used in earth sciences as it provides a means of quantifying the uncertainty of subsurface parameters (Sambridge and Mosegaard 2002). In this study, it will be applied to permeability and azimuth uncertainty of fractures. Azimuth in this case refers to the azimuth of the fracture of fracture network with respect to an imaginary line which connects the injection and production wells. A schematic representation of this is shown in Figure 3-7.

There are several variations of the Monte Carlo methods, the procedure followed for this study is outlined below.

1. Define a domain of input parameters (i.e permeability & azimuth values)
2. Randomly select inputs from this distribution
3. Perform multiple realisations with randomly generated parameters

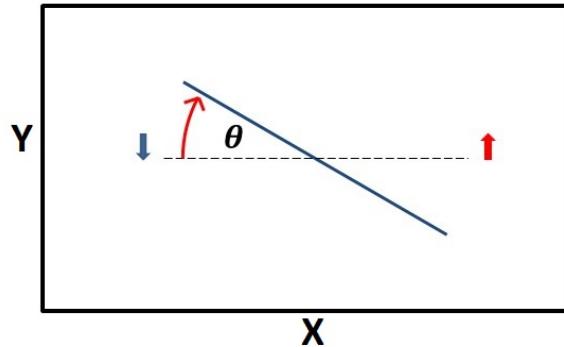


Figure 3-7: Schematic representation of fracture azimuth considered in this study. Red and blue arrow represents the injection and production well - not drawn to scale

4. Compile and analyse results

The generation of the distributions and random selection was performed using Matlab. The script used for this can be found in Appendix C-2-1. The generated values were written directly to a text file which was subsequently called by a Python script written to generate input files for multiple realisations (See Appendix C-1-2). The distributions and their parameters are shown in Figure 3-8

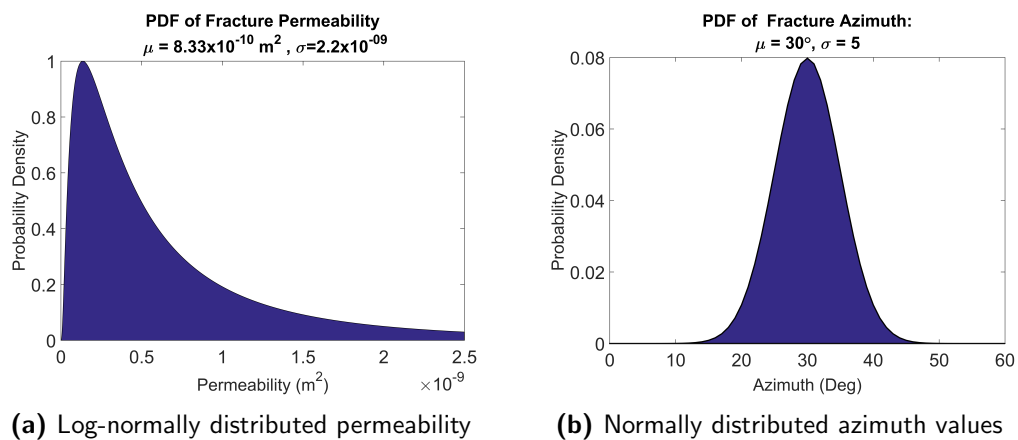


Figure 3-8: Probability Distributions generated using Matlab

3-4-1 Quantitative Analysis Approach

Typically, probability distributions are described using their mean and standard deviation. Some of the simulated results are characterised by a skewed distribution as they mirror the shape of the log-normally distributed input values. This skewness must therefore be taken into consideration when analysing the results of the experiment. In these cases, standard deviation is inadequate as it gives no information on the asymmetry. In cases where the output profiles are not evenly distributed around the mean value, the quantiles will be used to describe the distribution. Quantiles are less susceptible to long-tailed distributions.

The skewness of the distribution will be quantified for comparison purposes using the Pearson Mode Skewness, (Pearson 1894). Pearson described the skewness, S , of a distribution as a function of the mean, μ and mode, M (i.e., the value most likely to be sampled). The relationship follows,

$$S = \frac{\mu - M}{\sigma}, \quad (3-1)$$

where σ is the standard deviation of the distribution. This nonparametric skew is suitable to this application as its calculation does not require any knowledge of the form of the underlying distribution, it allows for a reasonable quantification of the results.

An additional metric which will be considered in the quantitative analysis is percentage decline. This is an intuitive value which is an expression of the normalised temperature decline as a percentage of the total decline over the lifetime of the reservoir. It is defined as follows,

$$\Delta T_N = \frac{T_i - T_f}{T_i - T_f} \times 100, \quad (3-2)$$

where subscripts i and f represent the initial and final production temperature respectively. This metric shows clearly the variations in rate at which the reservoir heat is depleted. According to this metric, smaller values indicate a greater extent of skewness.

Further visualisation of the results was achieved using histogram plots. The data was split into 25 bins for the generation of histogram and for brevity, the plots at 5, 15 and 30 years are considered. The binning of the data and generation of histograms was performed using Matlab statistical analysis functions. (See Appendix C-2-2)

Part II

Results and Analysis

Chapter 4

Observations

In this chapter the results obtained from a number of simulations will be documented. The primary metric for observing the influence of the fracture network parameters will be the production temperature profile over a 30 year period. The following sections will display a series of plots as well as reservoir maps and an initial qualitative description of the results.

4-1 Part I

4-1-1 Base Case I

In order to study the influence of the presence of a fracture in the reservoir, a reference point must be defined. This was achieved by performing a reservoir simulation where no fractures exist, purely rock matrix. The results are displayed in Figures 4-1 and 4-2. It can be observed

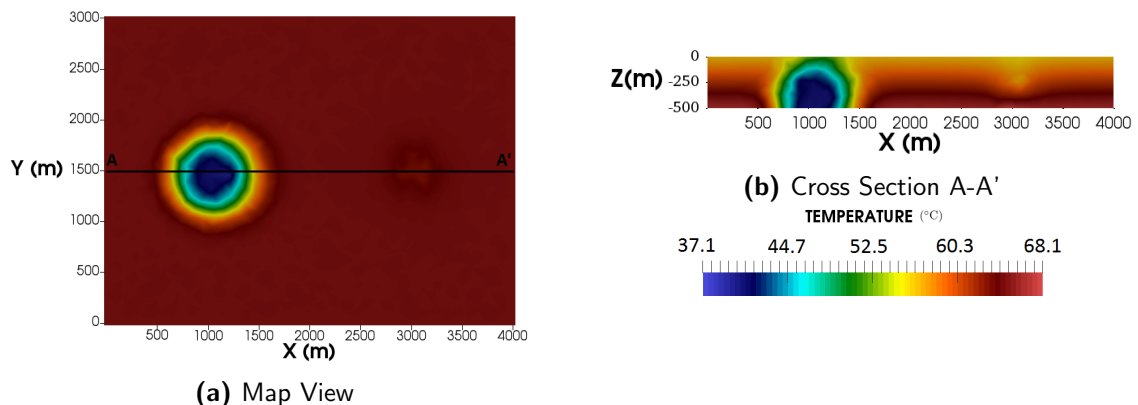


Figure 4-1: Matrix only base case showing reservoir temperature distribution after 30 years in map view and cross-section view

that the cold water front moves radially outwards from the injection well. The cold water

front moves at the same velocity and so a circular shape is maintained in the cold water front. In the cross section image (Figure 4-1b) the impact of production can also be observed. The temperature field lines curve downward around the well where the warm water is being produced. This cone of depletion becomes progressively wider as the reservoir life progresses. The temperature production curve seen in the figure above exhibits the typical depletion curve

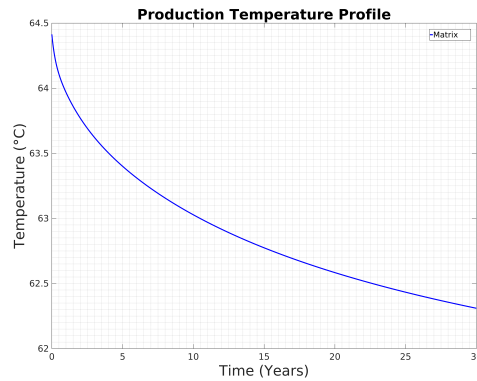


Figure 4-2: Temperature production profile for matrix only base case in Geometry II

for a geothermal doublet system. It can be seen from both the temperature distribution and the production curve that no thermal breakthrough occurs. The total drop in temperature that occurs is around 2 degrees. The curve also shows a steeper rate of depletion in the earlier stages of production which begins to slow after 10 years.

4-1-2 Permeability Study I

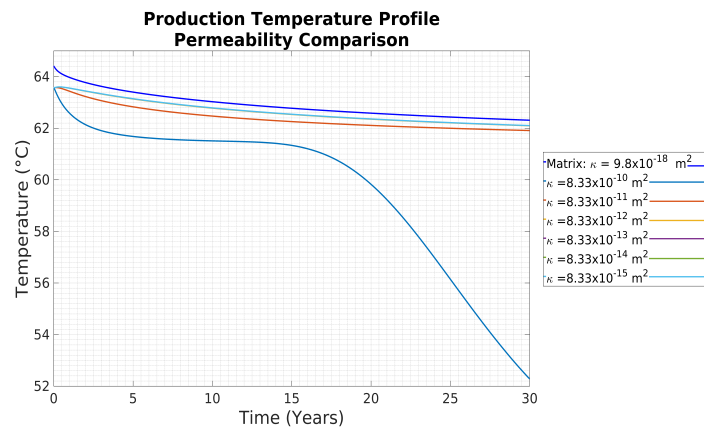


Figure 4-3: Comparison of production temperature profile for a varying values of permeability

The fracture permeability plays a key role in the influence that fractures have on the system efficiency. As discussed in Section 2-5, hydraulic conductivity of a fracture is a function of the permeability and therefore the fracture aperture. The effect of changes in the aperture was examined by running six simulations where the fracture permeability was varied by one order of magnitude in each successive case. The highest permeability considered was $8.33 \times 10^{-10} \text{ m}^2$, which according to the relationship shown in Equation 2-15, corresponds to an aperture value

of 0.0001 m. This can be considered a very open fracture. Figure 4-4 shows the contrast in the movement of the cold water front from injection toward production well. This image highlights the strong influence of aperture on the reservoir temperature distribution

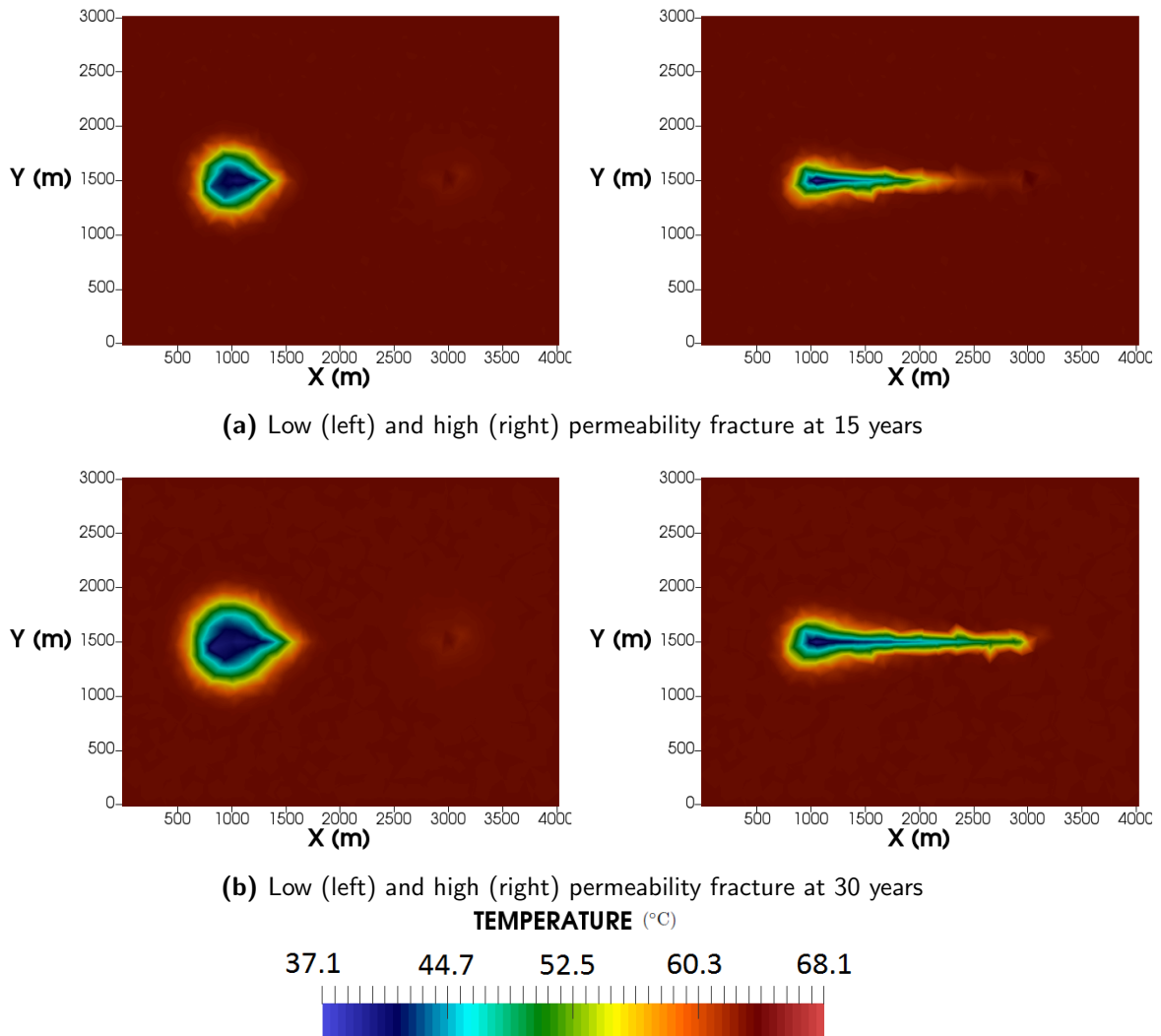


Figure 4-4: Map view of reservoir with single embedded fracture showing the contrast between low and high permeability. The snapshots at 15 and 30 years show that the heat transfer is confined to a smaller region around fractures when the permeability is higher

It can be observed in the figure that the cold water front advances further in the same period than the lower permeability case on the left. The shape of the cold water front is markedly different in the two cases, it can be seen for the high permeability case, the reservoir area that is involved in the heat transfer is confined and close to the fracture walls. In the lower permeability case it is observed that the water moves further outward into the matrix.

Another key observation is that for the higher permeability, thermal breakthrough occurs. The increased permeability results in higher velocity in the fracture and so the injected cold water moves more quickly toward the producing well. This can be further observed by the

shape of the temperature production profile shown in Figure 4-3. The high permeability case is characterised by the steepest decline in production temperature within the first five years, the rate of decline is relatively comparable between five to 15 years for the entire range of permeability values. Around the 17 year mark, the gradient of the production profile for the high permeability case considerably steepens for the high permeability case. At this point thermal breakthrough has occurred and the cooler water that has been injected has arrived at the production well. First signs of this breakthrough can also be seen in the upper-rightmost temperature distribution snapshot Figure 4-4

Finally, it can be seen that the production profile appears to approach the matrix case as the permeability is lowered toward the value of the matrix. The first shift from the high permeability case by one order of magnitude is the most drastic with a difference of up to 10°C in the late stages. However, the subsequent shifts are considerably smaller. The changes in permeability values below $8.33 \times 10^{-12} \text{ m}^2$ in fact had such smaller variations that the production profiles plot virtually on the same curve. This indicates a limitation in the implementation whereby there should be at least five to six orders of magnitude difference between fracture and matrix permeability for there to be a measurable difference.

4-1-3 Permeability Experiment

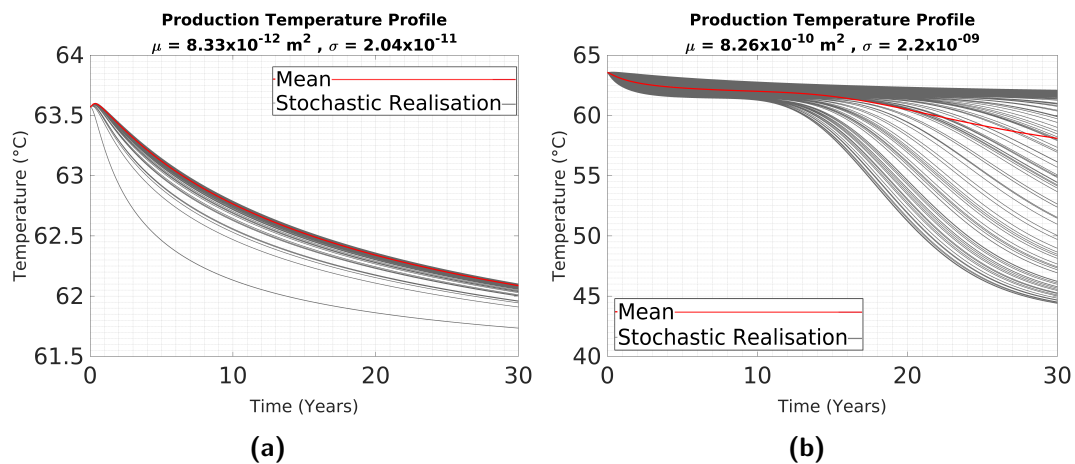


Figure 4-5: Production Temperature Profile of low (a) and high (b) permeability scenarios. The grey lines represent the distribution of 200 realisations. The contrast between the distributions shows the weight of the influence is dependent on the ratio of permeability between the fracture and the surrounding matrix. Average response is plotted in red.

As discussed in Section 3-4, 200 realisations were performed using permeability values randomly generated from a log normal distribution. The analysis was performed for both high and low permeability values in order to compare the effect of uncertainty in these different reservoir scenarios. The production temperature profiles and the associated distributions of the realisations are shown side by side in Figure 4-5. It can be seen that there is considerable uncertainty in the production for a reservoir scenario where the fracture permeability is high relative to the matrix. It is also noted that this uncertainty increases considerably with the life of the reservoir. This large uncertainty can be attributed to whether or not thermal

breakthrough occurs. This is therefore a factor that must be considered in planning of such a reservoir.

Another characteristic that can be observed is that the distribution of the production profiles are non-symmetrical about the mean. The skewed distribution can be attributed to the inherent skewness of a log-normally distributed permeability values. This implies a direct relationship between the fracture permeability distribution with the uncertainty of the possible production scenarios. It must be noted that this study considers one fracture with a constant permeability value. In reality, fracture permeability varies within the reservoir according to the stress regime and fracture orientation and this may result in a different or more dispersed behaviour. Additionally, it is assumed by this implementation that the fracture is represented by two parallel plates but in the subsurface permeability may vary along a single fracture due to surface roughness.

4-2 Azimuth Experiment

The azimuth of the fracture with respect to production (See Figure 3-7) can play a role in the flow path that is set up in the reservoir. There can be several different orientations of fractures within a reservoir which are indicative of present as well as past stress regimes. In this study, only variation in the azimuth with respect to the injection and production wells would be considered. The dip azimuth will be held constant at 90° representing a vertical fracture. The azimuth of hydraulically conductive fractures can be inferred from borehole seismic data but as many fractures are below seismic resolution this can be challenging. This data is also limited to the volume of rock around the wellbore and therefore uncertainty increases moving outward to the reservoir. Additionally, while there may be many orientations of fractures, the current stress regime can provide information on which fractures may be sufficiently open to conduct fluid within a reservoir. In all of the aforementioned scenarios there is inherent uncertainty in constraining the actual fracture azimuth.

The effect of this uncertainty was again investigated using a Monte Carlo approach described earlier. One hundred (100) values were randomly generated from a probability distribution of azimuth with the parameters $\mu = 30^\circ\text{C}$ and $\sigma = 5$. An average azimuth of 30°C was used as it is a common orientation of fractures found in many stress regimes. All rock and simulation parameters were held constant over 100 realisations (See Tables 3-1, 3-3). The only change made in each case was to the mesh file, a new mesh had to be generated for each new orientation of the embedded fracture. The results of the study are displayed in Figure 4-6. One clearly noticeable difference in this result from the plots shown in Figure 4-5 is that the initial temperature distribution in the reservoirs shows slight variations (i.e. all of the curves do not start at the same point at $t = 0$). It can be inferred from these results that the orientation of the fracture in the reservoir plays a role in the temperature distribution. The fluid in the fractures have lower conductivity than the surrounding rock matrix and therefore acts as insulation, so observed temperatures at the production well may be slightly higher or lower depending on the distribution of fractures in the vicinity.

It is also observed that the distribution of the temperature profiles appears to be more symmetrical about the mean value (red curve), particularly when compared to the previous permeability study. This follows from the earlier postulation that the degree of uncertainty of the

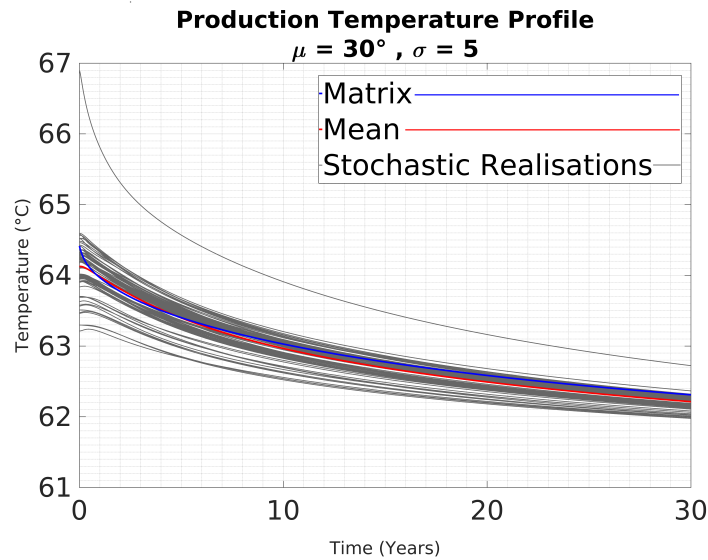


Figure 4-6: Plot of 100 temperature production profiles for azimuth uncertainty analysis, mean production profile shown in red and the matrix case shown in blue. Symmetrical distribution of profiles about the mean and variations in initial ($t = 0$) temperature distribution can be observed.

production profiles is directly related to the distribution of input parameters. The standard deviation is essentially constant over the life however there appears to be a little convergence of the distribution toward the end of the reservoir lifetime. This implies that there is more uncertainty in the early production years that can be attributed to fracture azimuth.

4-3 Part II

The second part of the study considers smaller reservoir dimensions. Rock and simulation parameters were mostly kept the same with only the exception of a change in the pumping rate which had to be lower due to the size of the reservoir. The pumping rate used was 0.05 m/s. This study considers three DFNs as shown in Figures 3-6 and 3-5. The single fracture case is also revisited in this geometry.

4-3-1 Base Case II

The matrix base case is again displayed as a reference for future results. In this case, very similar results can be observed as the cold water front once again moves radially outward from the point of injection. Figure 4-7 show a snapshot of the reservoir after 30 years of production.

The total drop in temperature in this case is smaller. This can be due to the influence of the pumping rate relative to the volume of the water. It was found that for higher pumping rates, the temperature drop was higher and also the curve became steeper. A plot comparing several pumping rates can be seen in the Appendix A-1. It can be seen from this plot that the behaviour of a geothermal system is very sensitive to the pumping rate as this determines the

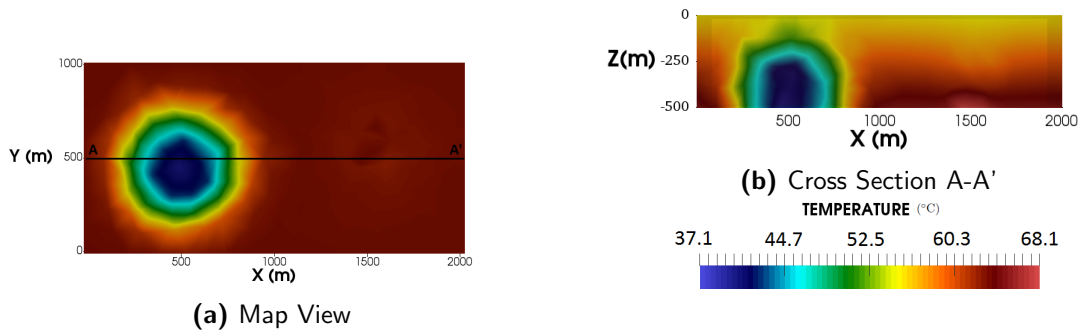


Figure 4-7: Matrix only base case showing reservoir temperature distribution after 30 years in map view(a) and cross-section view (b)

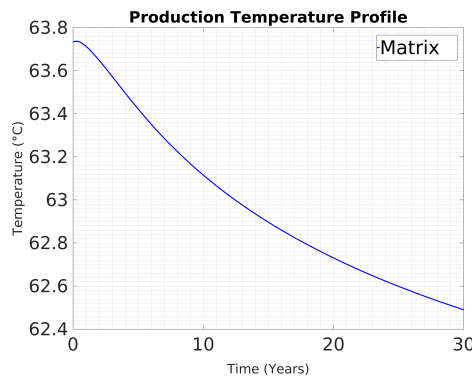


Figure 4-8: Temperature production profile for matrix only base case in Geometry II

volume of rock that is involved in the heat transfer process. The Pumping rate also affects the fluid velocity in the pores (Equation 2-5) and this influences the time in which thermal breakthrough occurs. As a result this must be held constant across all experiments in order to allow comparison. The temperature production profile can be seen in Figure 4-8. The curve shows a slightly different decline rate as observed in the first geometry. The lower rate can be also attributed to the reduction in the pumping rate.

4-4 Azimuth Study

An azimuth study was conducted to examine the effect of changes in the azimuth of a single fracture embedded in a reservoir. The value of the azimuth was varied from $0^\circ - 60^\circ$ in intervals of 10° . The geometries can be seen in Appendix A-2. This range of value are typically found in the subsurface and so the difference in the production profiles can give an indication of the effect of uncertainty in these values. The results of this study are shown in Figure 4-9. It is observed that the largest shift in the profile takes place when the azimuth changed from 0 to 10 degrees. Subsequent changes are relatively smaller. Additionally, the shift in production profiles are not equivalent over the entire lifetime and so the curves are not parallel. Consider the shift between 10 degrees to 20 degrees, there is a bigger shift in the temperature production at the early stages of the reservoir which gradually becomes smaller

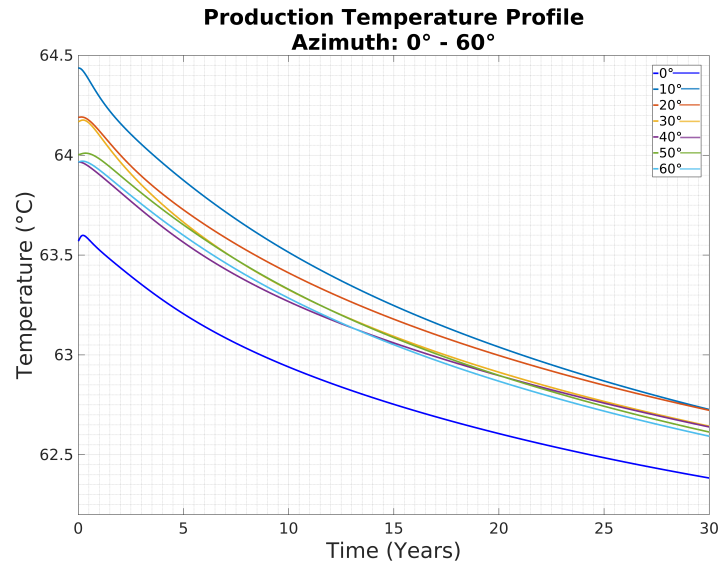


Figure 4-9: Comparison of temperature production profile for azimuth values from 0° – 60°

toward the end of the lifetime. There is an opposite trend observed for a shift between 20 degrees to 30 degrees. This trend does not appear to be preferential to any particular azimuth range. The production profiles for 40, 50 and 60 degrees all vary within 0.1°C of each other and this variation may fall within the error bars for the simulations. As a result these profiles can be considered to be virtually the same. This implies that at higher azimuth values the uncertainty in fracture orientation has a smaller effect on the production outcome. As a fracture becomes more perpendicular to the main flow direction, its influence on the heat transport process also diminishes. The amount of time that fluid is actually inside the fracture walls, and thus experiencing advective heat transport, is affected by the fracture orientation with respect to flow.

4-5 Permeability Study II

The effect of permeability uncertainty was further analysed in this reservoir geometry. In this section the results of 100 simulations would be examined. It was found from the previous study that the first 100 realisations sufficiently described the distribution and no significant information was gained by an additional 100. In this scenario a *DFN* is considered rather than a single fracture as in the first permeability uncertainty analysis. The fracture network *DFN-1* (Figure 3-5a) which contains 8 discrete fractures will be the first network examined. The values used for permeability were the same as the first experiment and so the mean and standard deviation of the input are the same.

The distribution of results seen with the low permeability fractures shows a similar behaviour to the single fracture case. Although there are more discrete fractures, the value of the permeability is closer to the matrix value and so the uncertainty in the input does not translate to a very high uncertainty in the simulation output. This principle appears to hold regardless of the fracture distribution. The contrast between the low and high permeability case is not as sharp as in the single fracture experiment. The very strong skewness of the distribution that

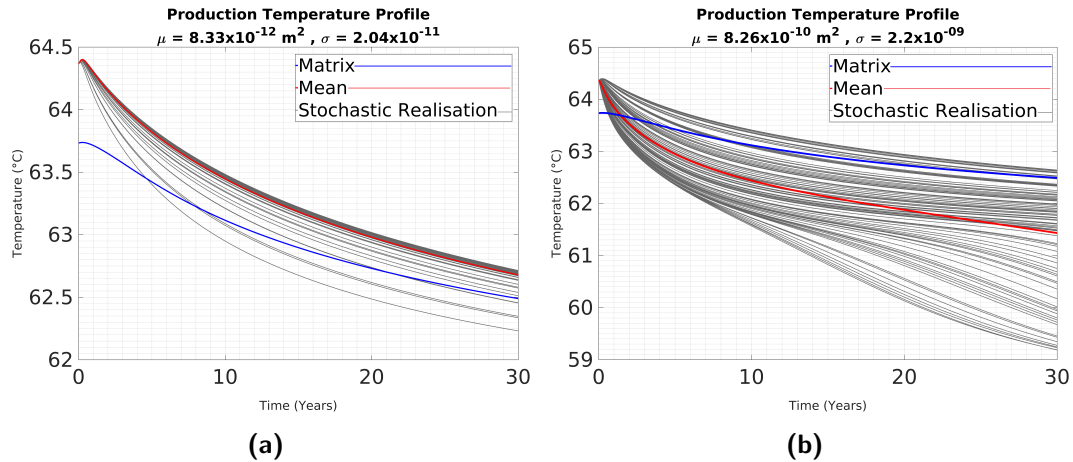


Figure 4-10: Production Temperature Profile of low (l) and high (r) permeability scenarios. The grey lines represent the distribution of 100 realisations. Average response is plotted in red.

was observed in the high permeability case was not evident when the same values were applied to the DFN. It can be observed in Figure 4-10b that the stochastic realisations appear to have a more even distribution. This can be attributed to the fact that there now exists several potential pathways for fluid to flow and thus the chances of thermal breakthrough occurring are reduced. This can also be observed in the reservoir snapshots displayed in Figure 4-11.

It can be observed in these plots that the flow path is very different. The images on the left show the progression of the cold water front being confined to an area of the matrix between two fractures. The flow of the cold water is in effect deflected away from the production well. In contrast to the single fracture case, after 15 years of production the cold water front although having advanced through the fracture network, has not approached the zone of the production well draw down. Between 15 and 30 years the cold water front begins to advance along a third fracture and a merger between the zone of draw down and the cold water front can be observed. In the case of the single fracture, this merger occurs much earlier between the five and 15 years. This experiment highlights the effect of the fracture distribution within the reservoir. The observations suggest that the orientation of the fracture network can exaggerate or stem the uncertainty associated with fracture permeability.

An interesting observation in this experiment is the position of the matrix production profile relative to the realisations. This is again an indication of the insulating effect of the fracture network in the matrix. The volume of the matrix rock surrounding the embedded fracture is smaller in the new geometry and so the insulation effect is more apparent. In the high permeability case (Figure 4-10b) the increased flow in the fracture results in more rapid depletion of the temperature. This can be seen in the steepness of the red average curve especially in the early time. The average profile also indicates a greater overall drop in temperature, more heat is extracted from the system when fractures are very open to fluid flow, the insulating effect is outweighed by the heat transfer. It is seen in the lower permeability case, that not as much heat is extracted from the system and the average profile is in fact at a slightly higher temperature than the matrix case.

The observations so far suggest that there is some interrelation between the effect of permeability uncertainty and fracture orientation or distribution in the reservoir. A fracture

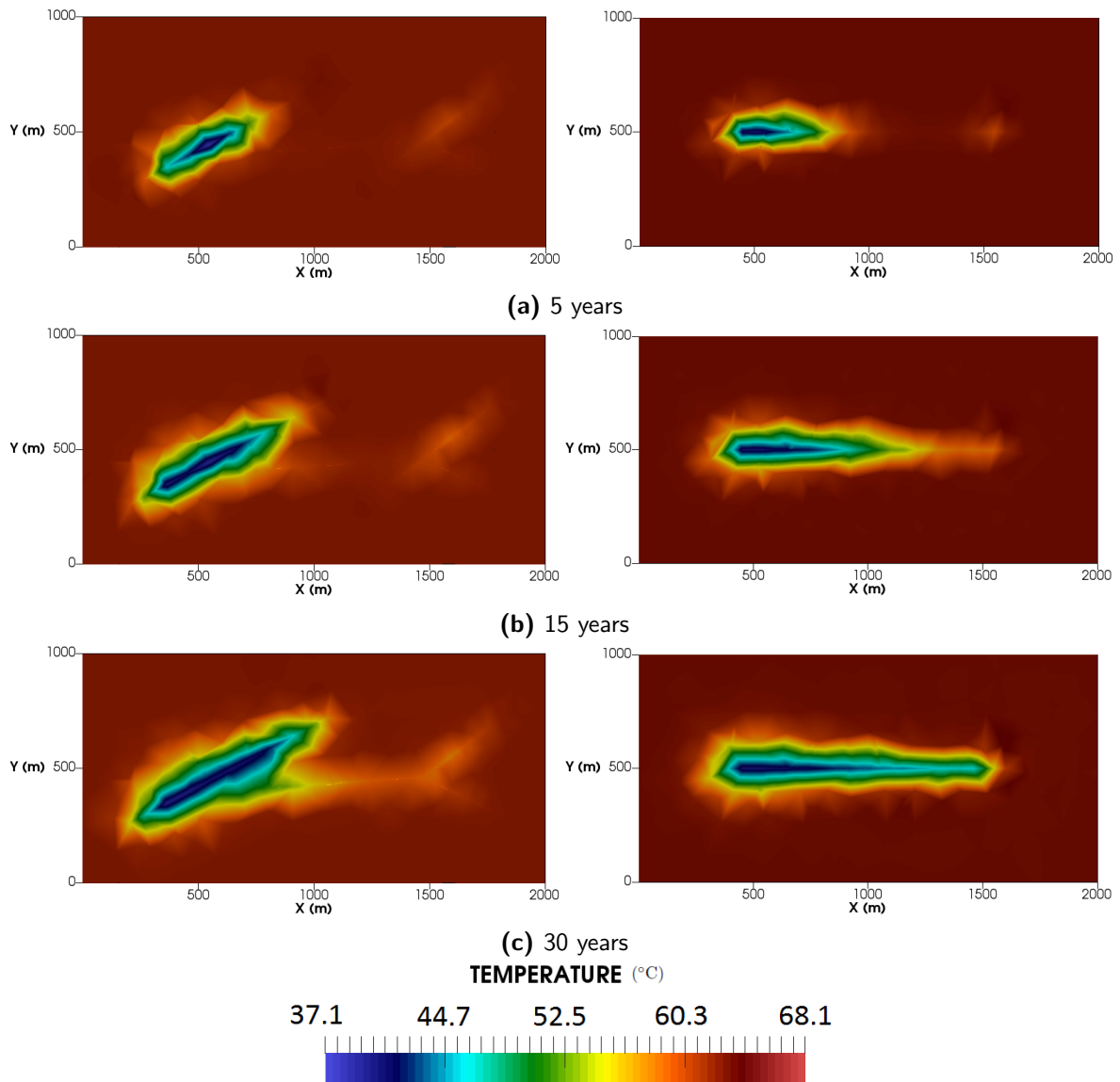


Figure 4-11: Comparison of flow paths for DFN-1 (left) and single fracture (right). Depth slices at 1900m

network orientation which is preferential to the main flow direction will result in more uncertainty with respect to expected production. Similar experiments were conducted with DFN-2 and DFN-3 in order to make a comparison. These networks generated with Petrel have different geometries but both contain several fractures including intersecting features. Therefore, they represent the most realistic scenarios examined in this study. The results of 100 simulations for the three fracture networks are shown in Figure 4-12. In these experiments the mean of the permeability distribution was $8.33 \times 10^{-12} \text{ m}^2$. The very high permeability was not considered in this experiment as this effect has been sufficiently observed. This experiment aims to investigate the fracture geometry and how this may affect the uncertainty. It can be observed that the distribution of the stochastic realisations becomes more narrow as the number of fractures in the network increases from DFN-1 to DFN-3. The contrast between

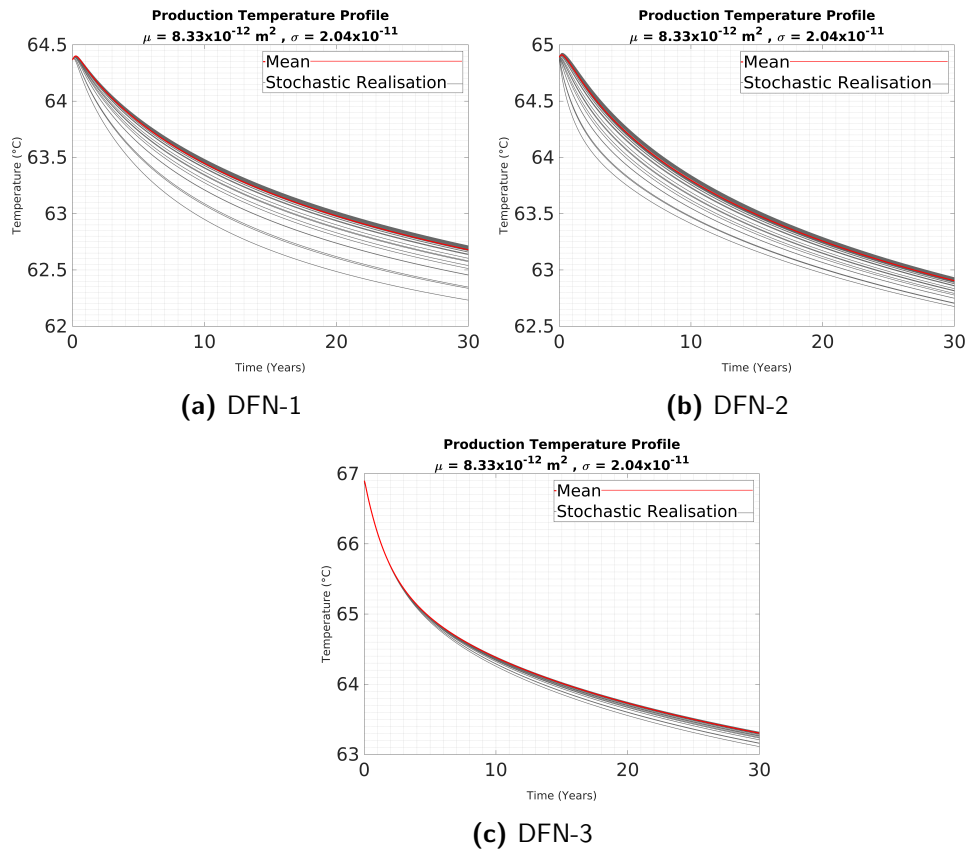


Figure 4-12: Contrast of the uncertainty associated with permeability in two different discrete fracture network models.

DFN-1 and DFN-2 is more subtle, however, the DFN-3 shows a very narrow distribution of production profiles. It is important to reiterate that in these experiments, all fractures in the network have the same value of permeability so the effect of the geometry is isolated in this case. Additionally, the same 100 values were used in the three experiments making them directly comparable. There appears to be a correlation between the fracture density and the permeability uncertainty. These observations suggest that when a more dense fracture network exists in the reservoir, the permeability uncertainty effect is diminished. This can be due to the increased number of flow paths that exists in a denser fracture network.

Another effect that can be observed is the change in the gradient of the average production profile. It becomes gradually steeper as the fracture density increases. An increased number of fractures in the reservoir results in more contact surface area between fluid and the rock matrix. A consequence of this is more rapid draw down or depletion of the heat in the reservoir. This can be seen more clearly in Figure 4-13. Again the contrast is subtle between the first two fracture networks but DFN-3 shows a markedly sharper decline in temperature, particularly in the first ten years of production.

4-5-1 Fracture Geometry and Temperature Distribution

It was hypothesized in the azimuth study of Part I that the temperature distribution in the reservoir appeared to be affected by the proximity of open fractures. A small experiment was conducted to test this effect, whereby the temperature production profile for varying reservoir scenarios would be compared. The four cases would be the matrix case and three DFNs. In each of these cases, the distribution of fractures is different, therefore, there should be varying effects on the temperature distribution.

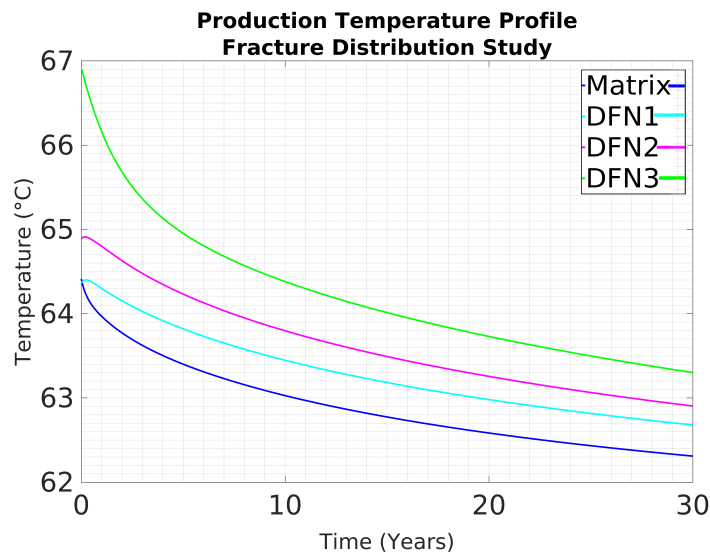


Figure 4-13: Temperature production profiles showing the influence of increasing number of fractures in the reservoir

The results of the experiment are shown in Figure 4-13. As hypothesized, the curves all have different initial temperature values at $t = 0$. The values range from 0.5 K – 3 K above the matrix case. The insulating effect of water present in the fractures appears to be proportional to the fracture density. In the case of DFN1 (8 fractures) we see a small increase in temperature of approximately 0.5 °C; whereas DFN3 (33 fractures) corresponds to an increase of up to 3 °C. The higher fracture count is also responsible for the noticeably steeper gradient of the decline in the case of DFN3. More fractures means that heat transport by advection becomes more dominant resulting in more rapid depletion of the heat in the system. These observations suggest that the distributions of fractures in the reservoir must be considered when planning the development of a geothermal system. Reservoirs are generally compartmentalized by fracture networks and the optimal placement of the production well can result in higher production temperatures. This is of course a trade off situation as the highly fractured compartment while having higher matrix temperatures may also mean a more rapid decline of temperature.

Dynamics of the Cold Water Front

The velocity of fluid moving through the rock matrix and fracture network is governed by Darcy's law. The fracture network largely controls the movement of the cold injected water through the reservoir. The orientation of the fractures can therefore determine how quickly the cold water may arrive within the zone of draw down of the production well. The zone of draw down around the production well can also be influenced by nearby fractures. In this section an overview of the movement of the cold water front in the three discrete fracture networks will be given.

The map views shown in Figure 4-14 are taken at the depth of the injection. DFNs 1 to 3 are displayed in the rows 1 to 3 respectively. It can be seen in the map views that the cold water front moves primarily along the direction of the fracture orientation and additionally in an area of the matrix just adjacent to the fractures. When comparing the first column of images at 10 years it is observed that the area invaded by the cold water is roughly the same. At the 20 year mark, the progression of the cold water front is more elongated in DFN-1 than the other networks. This is due to the fact that there are intersecting fractures at other orientations which allow the water to move outward and cover a larger area. It is also observed that in DFNs 1 and 3 there is a fracture which provides an almost direct channel between the injection and production wells. As a consequence, the temperature reduction around the production is observed to be greater in these two scenarios. In particular it can be seen in DFN-3 that the area of temperature reduction around the production well is the most extensive due to the surrounding fractures. At the final year of production, not very much has changed in the shape but it can be seen in DFN-3 that there is a much higher probability that thermal breakthrough may occur in these scenarios as a result of the fracture orientation. In the case of DFN-1, although there is an apparent connection between injection and production well, the prevalent direction of the fluid is not oriented toward the production well so the risk of breakthrough here will be less.

The corresponding cross sections are displayed in Figure 4-15 and give further perspective into the way the cold fluid invades the reservoir. The cross sections are all taken along the line connecting the injection to production wells. The variation in the invasion pattern can again be observed for the three different fracture networks. The variations in the temperature distribution throughout the reservoirs can also be appreciated from this perspective. It can be observed that in DFN-3 (3rd row) the temperature field in the reservoir is the most altered. Comparing the first and third fracture network it can be clearly seen how the orientation of the fractures can significantly influence how much heat is extracted. In the case of DFN-1 the zone of temperature disturbance around the production well is more narrow as can also be seen in the map view.

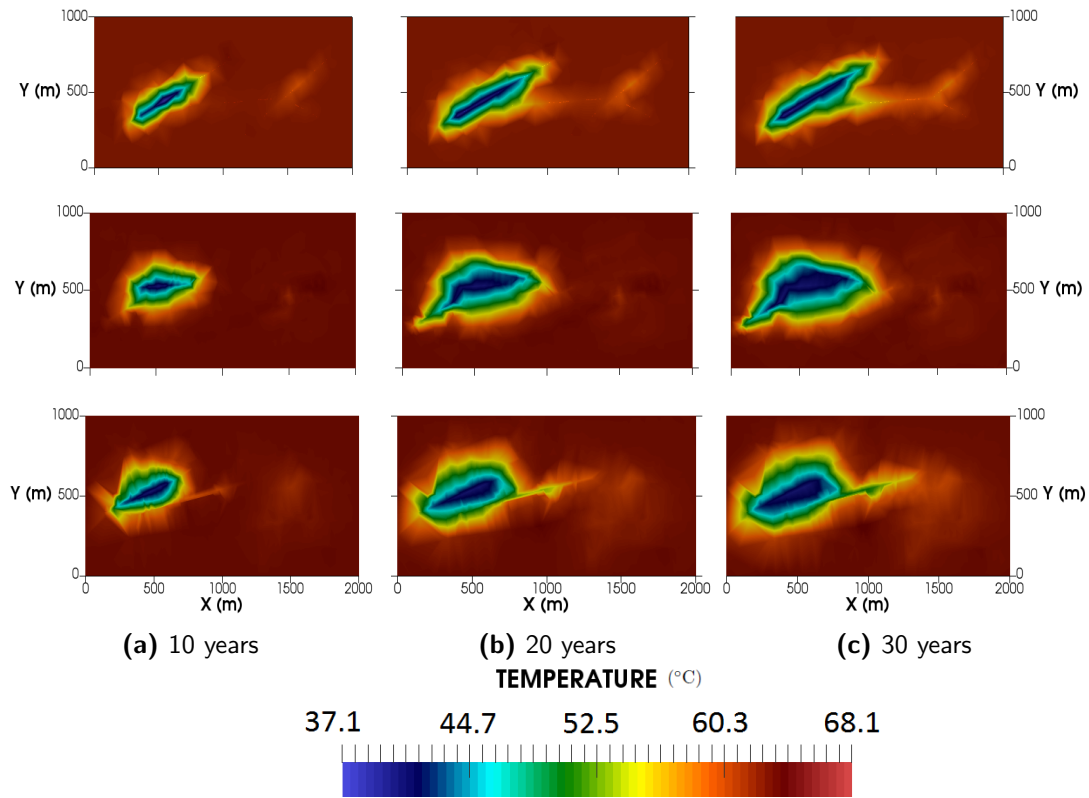


Figure 4-14: DFN-1 (1st row), DFN-2(2nd row), DFN-3(3rd row) Comparison of progression of cold water front in reservoir - Map View @ z = 1900 m

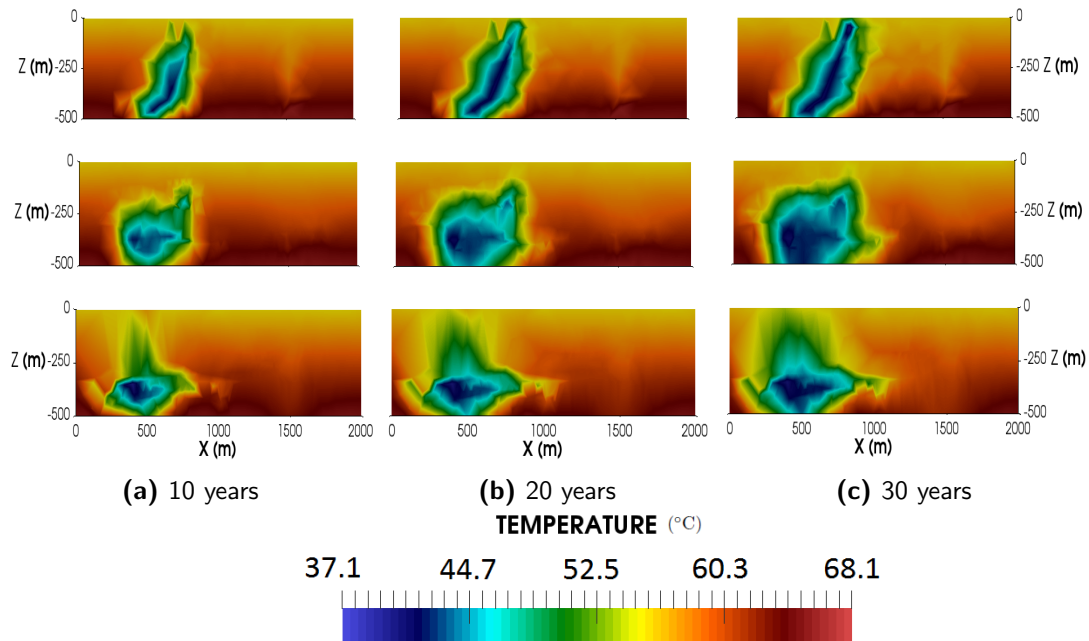


Figure 4-15: DFN-1 (1st row), DFN-2(2nd row), DFN-3(3rd row) Comparison of progression of cold water front in reservoir - Cross Section View

Quantitative Analysis

5-1 Geometry I Model

5-1-1 Permeability Uncertainty Analysis

The simplified case of a single fracture embedded in the rock matrix allows for a simplified and direct look at the influence of fracture permeability on the reservoir production. In this section the results of the permeability experiments will be more closely examined to determine what thresholds exist for the expected production given a particular scenario. The 20th and 80th percentile are chosen as markers in the distribution by which experiments can be compared. These values were obtained using Matlab, by combining all results into one matrix and using built-in statistical analysis functions. The distribution of experiment results is shown in Figure 5-1, including the 20th and 80th percentile thresholds plotted in magenta and green respectively. The position of the percentile lines plotted as dashed lines indicate the spread of the distribution. For instance, the 80th percentile should be interpreted as the line below which 80 % of the curves are plotted, likewise for the 20th percentile. It follows from the plots that the higher permeability scenario translate to a greater amount of uncertainty in production. The analysis confirms that for low permeability (Figure 5-1a), the range of possibilities is very confined and therefore the uncertainty of expected production is considerably lower. It can be seen in the plot that the 20th and 80th percentiles are very close together, meaning that the data is clustered around the mean. The values corresponding to the quantiles are summarized in Tables 5-1 and 5-2 over the period of production.

Time (years)	5	10	15	20	25	30
80th Percentile (°C)	63.14	62.79	62.54	62.36	62.22	62.10
20th Percentile (°C)	63.13	62.77	62.53	62.35	62.20	62.09

Table 5-1: Summary of temperature percentiles for Low Permeability

The data in the tables show clearly the contrast between low and high permeability scenarios. The 20th and 80th percentile were chosen as they can be useful metrics when describing the

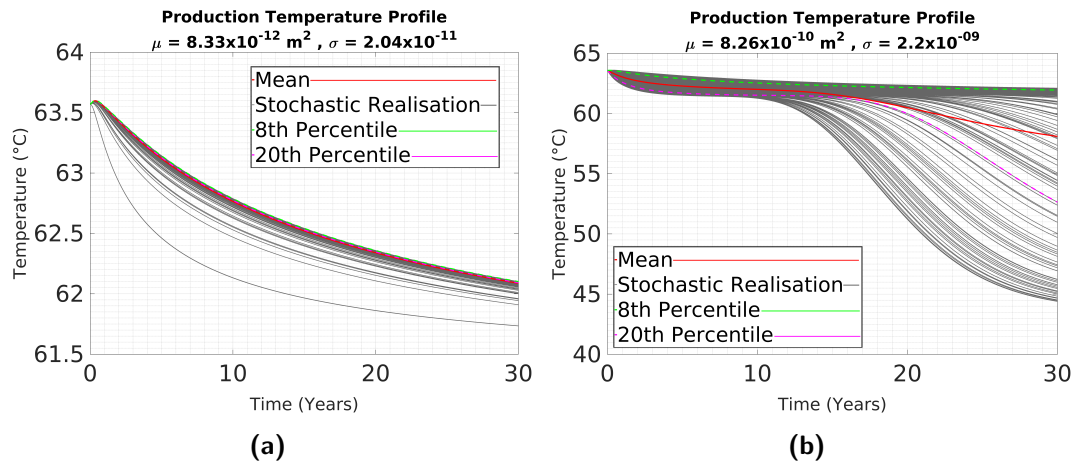


Figure 5-1: Production Temperature Profile of low (a) and high (b) permeability scenarios. The percentiles shown in green (80th) and magenta (20th) lines indicate the spread of the distribution which can be seen to increase with time.

Time (years)	5	10	15	20	25	30
80th Percentile (°C)	62.89	62.53	62.31	62.15	62.03	61.94
20th Percentile (°C)	61.69	61.51	61.36	59.98	56.47	52.64

Table 5-2: Summary of temperature percentiles for High Permeability

performance of a geothermal system. It can be seen that for the high permeability case, the range between the percentiles increases with the life of the reservoir. This must therefore be taken into consideration in the planning of such a reservoir. In the 10th year of production, the results indicate a 20 % chance that the temperature will be 61.51 °C or lower. The figure drops to 52.64 °C in the final year for the high permeability case whereas for the low permeability, this 20 % threshold sits at 62.09 °C. This represent an approximate difference of 10 °C between the two scenarios.

Comparing Decline Rates

Finally the rates of the heat production in the reservoir can also be very useful in well planning. The percentage decline as described in Equation 3-2 gives a quantitative perspective on how rapidly the heat in the reservoir is depleted over the production life cycle. It was calculated for the results of the experiment and the resulting trends are shown in Figure 5-2. The spread of these trends is also proportional to the uncertainty discussed earlier, so as expected, the high permeability case shows a wider range of possible trends. The low permeability case is very comparable to the matrix case, however, although the curves have a similar locus, it can be seen that in the early stages of production there is a greater difference in the percentage of the heat that is produced in the matrix and single fracture case. The difference gradually reduces until the later stages, after roughly twenty years of production there is little difference between the matrix and low permeability case. This shows that in the long run, a low permeability fracture on average exhibits behaviour similar to the matrix in terms of heat transfer.

In both cases it can be seen that for any given time, a higher percentage of the heat is

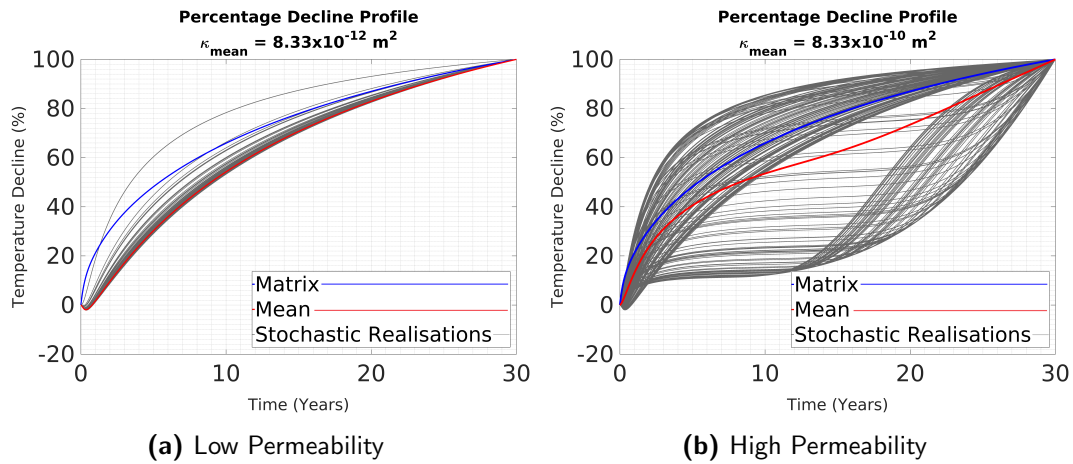


Figure 5-2: Percentage Decline plot of low (a) and high (b) permeability scenarios including the matrix decline rate (blue) for comparison. The average trend is plotted as a bold red line. It can be seen that the reservoir heat is depleted at a different rate in the cases where a fracture is present

depleted in the matrix case. The high permeability case shows a slightly different trend. In many cases, a greater percentage of the heat is depleted when a very open fracture exists, and in the early stages the average decline trend (red) and the matrix case (blue) are close. The average curve diverges somewhat from the matrix case and becomes less steep. This shape reflects the influence of scenarios where thermal breakthrough occurs. When this takes place, the thermal decline curve is characterised by a relatively flat gradient during the early period of production. This is because a substantial drop in temperature follows once thermal breakthrough has occurred. The results show that thermal breakthrough can significantly alter the production trend and increase the uncertainty.

Skewness

The skewed nature of the distribution must also be considered as it means that a higher weighting can be applied to some production scenarios when planning a reservoir. In a practical application, the skewness can indicate the likelihood of a scenario that is above or below the mean. These values are summarized in Tables 5-3 and 5-4 for the low and high permeability scenario respectively. The results show that in the high permeability case, the early stages of production are only slightly skewed with values just greater than one. The skewness increases around the middle of the reservoir life followed by a slight decrease in the final stages of production. The low permeability in contrast has a fairly constant skewness value over the life of the reservoir. The value is also very high, a result which confirms earlier observations. The high skewness is reflective of a very low standard deviation which is exhibited by the low permeability fracture scenario.

The distribution of the results and the implications of the skewness can be best represented graphically by histograms shown in Figure 5-3. The mean is temperature for each year is shown in red, the histograms show that given a particular mean expected value, the skewness implies that higher production values carry more weight in the distribution

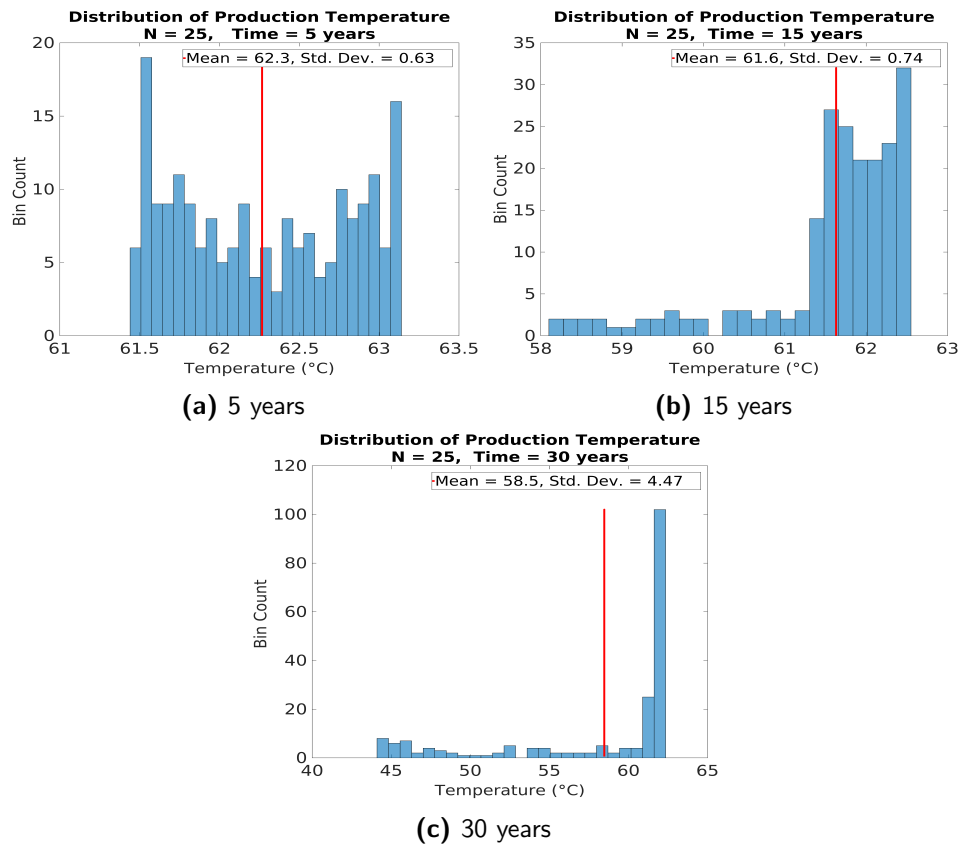


Figure 5-3: Distribution of production profiles for high permeability fracture scenario at 5, 15 and 30 years.

Time (years)	5	10	15	20	25	30
Average Temp. (°C)	63.12	62.77	62.52	62.34	62.20	62.09
Mode (°C)	62.46	62.13	61.97	61.86	61.79	61.73
Standard Deviaton	0.08	0.08	0.07	0.06	0.05	0.04
Skewness	8.32	8.16	8.09	8.02	7.95	7.88

Table 5-3: Statistic Summary: low permeability single embedded fracture

Time (years)	5	10	15	20	25	30
Average Temp. (°C)	62.28	62.00	61.58	60.48	59.15	58.09
Mode (°C)	61.50	61.25	58.14	51.20	46.31	44.39
Standard Deviaton	0.55	0.48	0.98	2.94	4.84	5.93
Skewness	1.42	1.57	3.49	3.15	2.65	2.31

Table 5-4: Statistic Summary: high permeability single embedded fracture

5-1-2 Azimuth Uncertainty Analysis

In this section, the azimuth experiment discussed in Section 4-2 will be further analysed. In Figure 5-4a the results of the experiment can be seen plotted along with the standard

deviation. The matrix case is also plotted in blue as a reference point. It can be seen in this plot that the matrix case falls within the bounds of the standard deviation which suggests that an embedded fracture in this scenario may not have a significant influence on production. The results also show that the distribution is more broad at the beginning of the reservoir life and becomes more narrow toward the end of the thirty year period. This suggests that uncertainty in production related with fracture azimuth is greater in the early stages whereas the late stages of production can be better constrained. It is important to note that the values of azimuth used in the experiment were randomly selected from a normal distribution, as described in Figure 3-8b, and the results also display a normal distribution. The normalized percentage decline is also shown in Figure 5-4b. It can be seen that the production rates are evenly distributed around the mean and in all cases, except one outlier, the normalized decline in temperature is less in the fracture case.

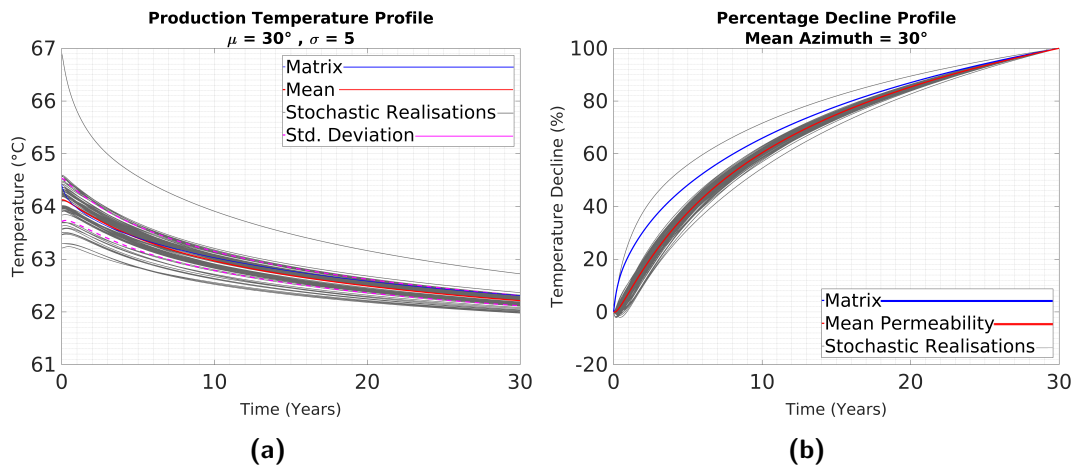


Figure 5-4: (a) Experiment results including mean trend in red and standard deviation as dashed magenta lines. The distribution is symmetric about the mean (b) Normalised percentage decline

The uncertainty related to the fracture azimuth shows a decreasing trend over the life of the reservoir, this behaviour is summarised in Table 5-5. It can be seen at five years after the start of production, the uncertainty is characterized by a standard deviation of 0.23 and this value drops to 0.15, a 34 % drop by the fifteenth year. In the final year of production the standard deviation is 0.10, just below half of its original value. The reduction in uncertainty over time is clearly reflected in the data.

Time (years)	5	10	15	20	25	30
Average Temp. (°C)	63.40	62.97	62.69	62.49	62.34	62.21
Mode (°C)	63.46	63.04	62.76	62.56	62.40	62.27
Standard Deviation	0.23	0.18	0.15	0.13	0.11	0.10

Table 5-5: Statistical summary of Azimuth uncertainty analysis over the life of the reservoir

5-2 Geometry II Model

5-2-1 Permeability Uncertainty Analysis

In this section, the results of the stochastic permeability experiment performed on DFN-1 (Figure 3-5a) will be analysed. The results indicate a different behaviour from the single fracture case. It must be reiterated that the random values from the distribution were the same for all the permeability experiments. In the case of a fracture network, it can be seen that the distribution of the production profiles is less skewed in the low permeability case and considerably less so in the high permeability case. The results for both low and high permeability are shown in Figure 5-5.

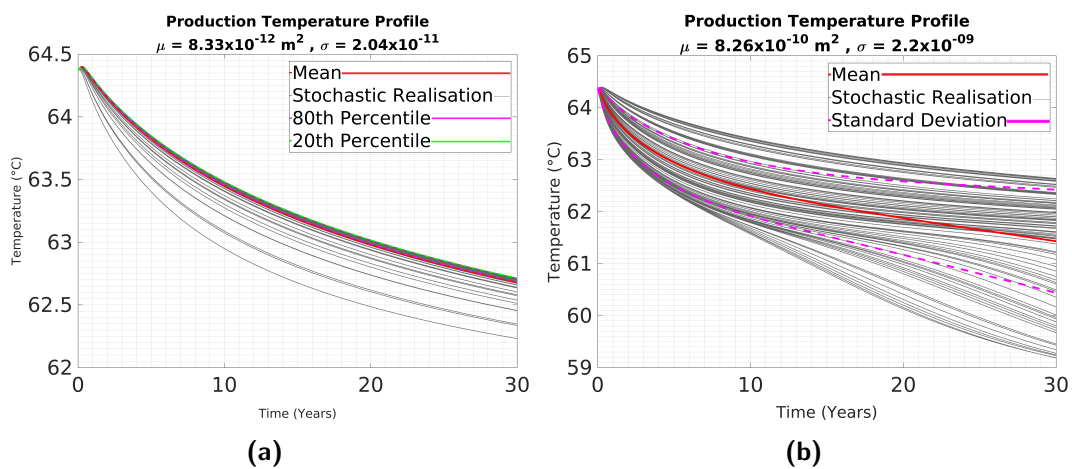


Figure 5-5: Production Temperature Profile of low (a) and high (b) permeability scenarios. Data shows greater contrast between the distributions in the low and high permeability scenarios when a DFN is involved as opposed to a single embedded fracture.

In the case of the low permeability the distribution is still skewed and so the percentiles must still be used for a meaningful graphical display of the results. It can be seen that there is a virtually negligible change in the difference between the percentiles over time which indicates a constant uncertainty with time. The same fracture network was assigned a high permeability and the distribution obtained was more symmetric. For this reason, the standard deviation is included in Figure 5-5b. It can be seen by the diverging trend of the standard deviation bounds that the uncertainty increases with the life of the reservoir. This behaviour was also seen in the first geometry and represents a key finding of this study. The results consistently show an increased uncertainty related to fracture permeability as the life of the reservoir increases. This increase is a characteristic of the higher permeability fractures.

The summary of the percentiles are shown in Tables 5-6 and 5-7. Again, the difference is very subtle in the low permeability case and relatively larger for high permeability. It can also be seen in the results that percentiles in the high permeability case occur consistently at lower temperatures than their low permeability counterparts. This is in keeping with the observation that reservoir temperature decreases faster for more open fractures. The difference between the 80th percentiles is small, on average 0.5 °C. The lower 20th percentiles are further apart, on average 1.5 °C.

Time (years)	5	10	15	20	25	30
80th Percentile (°C)	63.85	63.48	63.22	63.02	62.85	62.71
20th Percentile (°C)	63.83	63.45	63.19	62.99	62.82	62.68

Table 5-6: Summary of production temperature percentiles for DFN-1 with low permeability

Time (years)	5	10	15	20	25	30
80th Percentile (°C)	63.40	62.95	62.68	62.49	62.34	62.23
20th Percentile (°C)	62.48	61.92	61.61	61.33	60.98	60.49

Table 5-7: Summary of production temperature percentiles for DFN-1 with high permeability

Skewness

As discussed early, the production profile for geothermal doublet systems in a fractured reservoir is sensitive to a number of interdependent factors such as fracture distribution and orientation as well as production parameters such as pumping rate and reservoir volume. As a result comparison between the two geometries in this study must be approached with caution. Considering this, the single fracture case was also studied for this smaller geometry. The stochastic study was performed with 100 realisations using the same random permeability values. The results are not discussed at length here as they display the same behaviour as observed in the first geometry. However, it is important to note that since the same behaviour is observed in the single fracture case, the reduction in skewness of the distribution observed can be attributed to the increased complexity of the fracture network. An overview of the results of the single fracture case as well as a full summary of the statistics can be seen in Appendix A-3. The skewness of the distribution exhibited in the single fracture case

Time (years)	5	10	15	20	25	30
Average Temp. (°C)	63.82	63.45	63.18	62.98	62.82	62.68
Mode (°C)	63.40	62.95	62.68	62.49	62.34	62.23
Standard Deviaton	0.07	0.09	0.09	0.09	0.09	0.08
Skewness	5.66	5.58	5.53	5.48	5.43	5.40

Table 5-8: Statistic Summary: DFN-1 with low permeability

Time (years)	5	10	15	20	25	30
Average Temp. (°C)	62.95	62.44	62.12	61.88	61.65	61.43
Mode (°C)	62.35	61.57	60.83	60.13	59.58	59.19
Standard Deviation	0.45	0.52	0.59	0.71	0.85	0.99
Skewness	1.32	1.67	2.18	2.47	2.45	2.26

Table 5-9: Statistic Summary: DFN-1 with high permeability

appears to be moderated by the inclusion of a fracture network in the model. This can be attributed to the fact that more fractures mean that there are more possible pathways for the flow of fluid and the heat transfer process is more distributed throughout the reservoir. The reduced skewness can be clearly seen in the data summarized in Tables 5-8 and 5-9. The

results show a skewness value of 2.18 at the fifteen year mark for a highly permeable fracture network, this value corresponds to a 10 % reduction of the value in the single fracture case for the same time (Table A-4). There is an apparent deviation from this trend in the later stages of the reservoir life for the high permeability case, the skewness of the single fracture case is observed to be less than the fracture network case. This can be related to the fluid flow path in the fracture network. The comparison of the standard deviation between the low and high permeability cases (Tables 5-8 and 5-9) show that for high permeability, the standard deviation is on average six times more than the lower permeability case. The trend of the standard deviation in each case over the reservoir life shows different characteristics. In the case of high permeability, the results show that from the fifth year to the final year of production, there is an increase of 220 % in the standard deviation. This clearly represents the drastic increase of uncertainty with time. The low permeability case on the other hand shows a virtually constant value of uncertainty over the period.

5-2-2 Comparing the Discrete Fracture Networks

In this section a further investigation of the role of fracture distribution on the permeability uncertainty will be performed. The stochastic experiment was also conducted on DFN-2 and DFN-3 which contain 28 and 33 discrete fractures respectively. The fractures are of varying orientations but roughly aligned with the production direction, as shown in Figure 3-6. The results of the experiments are shown in Figure 4-12 where it was observed that as the fracture count increased, the distribution appeared to become more narrow. The shift is more drastic between the second and third networks. These findings are summarised in the Tables 5-10 and 5-11 below for every five year interval over the life of the reservoir. The summary of DFN-1 is shown in Table 5-8.

Time (years)	5	10	15	20	25	30
Average Temp. (°C)	64.23	63.80	63.49	63.26	63.06	62.90
Mode (°C)	63.76	63.41	63.16	62.97	62.81	62.67
Standard Deviaton	0.10	0.09	0.07	0.07	0.06	0.05
Skewness	4.70	4.52	4.44	4.40	4.37	4.33

Table 5-10: Statistic Summary: DFN-2

Time (years)	5	10	15	20	25	30
Average Temp. (°C)	64.95	64.38	64.01	63.73	63.50	63.30
Mode (°C)	64.89	64.25	63.85	63.55	63.31	63.11
Standard Deviaton	0.01	0.02	0.03	0.03	0.03	0.04
Skewness	5.59	5.57	5.55	5.52	5.48	5.43

Table 5-11: Statistic Summary: DFN-3

The results show different behaviours of the standard deviation or uncertainty over time. In DFN-1 the value is essentially constant over the thirty year period, whereas DFN-2 exhibits a reducing trend in the uncertainty. The opposite is seen in DFN-3 where the uncertainty increases slightly with time, similar to the single fracture case. The skewness values are very

comparable between the first and third fracture networks, however the second network shows slightly lower values. This can be related to the fluid flow paths in the networks. It can be postulated from these results that DFN-3 contains a preferential flow path due to the specific orientation of the fractures. As a result of this, it displays similar characteristics to the single fracture case in terms of skewness and increasing uncertainty in production profile with time. In DFN-2 we see lower skewness values and also a decreasing uncertainty with time. Considering the distribution of the fractures in the networks, there is indeed a higher density of fractures directly between the injection and production wells in DFN-3 when compared to DFN-2, (See Figure 3-6). It is therefore reasonable to assume that a more direct preferential flow path may exist in DFN-3.

Fracture Geometry and Temperature Distribution

The effect of the distribution of fractures in the reservoir was investigated in Section 4-5-1. The normalised percentage decline for this experiment is plotted in Figure 5-6 and it allows for a comparison of the depletion of the reservoir heat for different fracture networks.



Figure 5-6: Normalised decline plots showing comparison of results from three fracture networks and the matrix case.

Time (years)	5	10	15	20	25	30
Matrix (%)	24.99	49.66	67.27	80.62	91.24	100.00
DFN-1 (%)	32.39	54.50	70.13	82.16	91.87	100.00
DFN-2 (%)	33.17	55.08	70.46	82.31	91.94	100.00
DFN-3 (%)	54.12	70.03	80.25	88.11	94.56	100.00

Table 5-12: Summary of normalised percentage decline for three discrete fracture networks and matrix case

The results show a consistent increase in the decline rate with the number of fractures. DFN-3 shows the most rapid depletion with more than 50 % of the total temperature decline already taking place after 5 years of production. The successive decline in the later years is slightly

less steep than observed in the other networks. The first and second fracture networks show a very similar trend which can be attributed to similarities in the fluid flow path in both networks.

Chapter 6

Discussion

In this study, a discrete fracture network model approach was used to analyse the effects of fracture parameter uncertainty on production from a geothermal reservoir. The fracture permeability emerged as the dominant factor which influences this uncertainty. The dependency of the statistics of simulated results on the distribution of the input parameters was evident in the results obtained. I found that a sample size of 100 realisations was sufficient to make a statistical analysis of a particular set of input parameters, however, in this implementation, every fracture in the network was assigned the same permeability value. A more realistic approach would require individual fractures being assigned to differing permeability values from a distribution. Nonetheless, the comparison between the single fracture case and a discrete fracture network revealed that the presence of a preferential or direct pathway between the injection and production well results in a more skewed distribution of simulated results. This result is an indication that this stochastic study of a fracture network has the capability to reveal whether or not a preferential pathway exists in a fracture network. Additionally, the existence of similar flow paths in differing fracture networks may give statistically similar simulation results; this can be a means of comparing different scenarios.

The fracture distribution in the reservoir was also observed to influence the temperature field due to the insulating effect of the fluid. During the production lifecycle of a reservoir, the stress field is altered and this change can also affect the hydraulic aperture of fractures and the heat transport process. In this study, such mechanical processes were not coupled with the heat transport and fluid flow problem and it is essential for future studies that information on the 3D mechanical properties be incorporated. The study of the effect of fracture azimuth produced a range of production temperatures that was very narrow and in some cases very close to the absolute error of the numerical method and so these relationships must be approached with caution. The azimuth uncertainty analysis showed a different behaviour to the permeability whereby there was a reduction in the uncertainty with time. The study of fracture geometry parameters such as length and orientation could not be addressed in this study due to challenges with generating a finite element mesh for complex geometries. Alternative approaches such as stochastic generation of fractures consistent with local stratigraphic orientation, (Borghini et al. 2015); or the use of specialised simulators such

as Golder Associates FracMan DFN code for fracture generation as applied by [Doe et al. \(2014\)](#) can be considered to incorporate more realistic fracture geometries in future studies.

The normalised percentage decline was introduced as a metric to compare the rate of temperature decline in different productions scenarios in this study. Varying metrics exists such as the commonly used dimensionless time and temperature first introduced by [Gringarten and Sauty \(1975\)](#). The normalised percentage decline is a simple metric and the trend of this plot over time can be useful in planning a geothermal doublet system as it gives quantitative insight into how rapidly the temperature will decline over the course of the reservoir.

Chapter 7

Conclusion

The primary objective of this study was to examine geothermal doublet systems, considering the effect of uncertainty in fracture network characteristics and how they translate to uncertainty in production from the reservoir. The problem was approached using a discrete fracture network modeling method whereby fractures were represented as discrete elements embedded in the rock matrix. Several numerical simulations were conducted for a reservoir life period of thirty years including various fracture permeability, azimuth and distribution scenarios. Qualitative as well as quantitative analysis of the results indicate that fracture permeability is the parameter which has the most influence on the uncertainty related with production trends from a geothermal system. The distribution of the fractures within the reservoir proved to be more influential on the heat distribution in the reservoir.

Initial observations indicate that fracture network permeability plays a major roll in the total amount of heat that can be extracted from a geothermal system as well as the rate of the depletion. More permeable or hydraulically open fractures result in a more rapid depletion of reservoir heat. As fracture permeability increases, the possibility for the occurrence of thermal breakthrough also increases. This is an undesirable scenario as it drastically reduces the efficiency of the system with a sharp decline in production temperatures. The uncertainty of possible production scenarios is also sensitive to the degree of fracture permeability. When fractures are more open, the data shows that the range of outputs is considerably wider than for a lower permeability. This uncertainty can be very broad depending on whether or not there is a possibility of thermal breakthrough occurring in a particular production scenario, an additional negative side effect of thermal breakthrough. An important consideration that defines the production scenario is of course the pumping rate. An increased pumping rate results in a more rapid decline of temperature as fluid experiences a higher flux through the medium according to Darcy's law.

It was also observed that the fracture distribution within the reservoir can influence the effect of permeability uncertainty. The results of the permeability uncertainty analysis indicates that a fracture orientation which is preferential to the main flow direction will result in more skewed distribution of simulated results. High skewness in distribution of production profile resulting from a Monte Carlo approach can be a possible indication of the existence of a

preferred pathway. Otherwise, the simulation results would be more evenly distributed. This was observed by the similarity in the statistics of the single fracture case to one discrete fracture network which contains a more direct pathway of interconnected fractures between the injection and production wells.

There is an insulating effect of fluid filled fractures in the reservoir. Fractures can be thought of as thin columns of fluid surrounded by the rock matrix. The fluid, typically water, has a much higher heat capacity than the surrounding rock and therefore is a poor heat conductor. As a result, blocks of rock bounded by fluid filled fractures experience some insulation. This was seen in slightly higher temperatures when the production well was in the vicinity of a fracture or multiple fractures. The consideration of fracture distribution in the reservoir and how the aquifer is compartmentalized by the fracture network is therefore very important in planning a production scheme.

The rate of cooling occurring at the production well is not the only metric by which the performance of a geothermal system can be judged. In most cases a faster cooling trend is undesirable, however other criterion such as net power capacity or power generation over time can be more meaningful in some applications. The cooling rate was a reasonable metric in the scope of this study, but further studies may consider other metrics which represent a more comprehensive overview of the reservoir performance. The uncertainty related to the distribution of fracture length was not explicitly examined in this study. It would require further stochastic analysis with many more fracture networks to obtain a sufficient amount of data from which trends can be observed.

Bibliography

- Berkowitz, B. (2002). Characterizing flow and transport in fractured geological media: A review. *Advances in water resources*, 25(8):861–884.
- Berkowitz, B., Bour, O., Delay, P., and Odling, N. (2000). Scaling of fracture connectivity in geological formations. *Geophysical Research Letters*, 27(14):2061–2064.
- Blum, P., Mackay, R., and Riley, M. S. (2009). Stochastic simulations of regional scale advective transport in fractured rock masses using block upscaled hydro-mechanical rock property data. *Journal of Hydrology*, 369(3):318–325.
- Borghi, A., Renard, P., Fournier, L., and Negro, F. (2015). Stochastic fracture generation accounting for the stratification orientation in a folded environment based on an implicit geological model. *Engineering Geology*, 187:135–142.
- Courant, R., Friedrichs, K., and Lewy, H. (1928). Über die partiellen differenzgleichungen der mathematischen physik. *Mathematische annalen*, 100(1):32–74.
- Dershowitz, W. S., Herda, H. H., et al. (1992). Interpretation of fracture spacing and intensity. In *The 33th US Symposium on Rock Mechanics (USRMS)*. American Rock Mechanics Association.
- Doe, T., McLaren, R., and Dershowitz, W. (2014). Discrete fracture network simulations of enhanced geothermal systems. In University, S., editor, *39th Workshop on Geothermal Reservoir Engineering*.
- Dorn, C., Linde, N., Le Borgne, T., Bour, O., and De Dreuzy, J.-R. (2013). Conditioning of stochastic 3-d fracture networks to hydrological and geophysical data. *Advances in Water Resources*, 62:79–89.
- Geuzaine, C. and Remacle, J.-F. (2009). Gmsh: A 3-d finite element mesh generator with built-in pre-and post-processing facilities. *International Journal for Numerical Methods in Engineering*, 79(11):1309–1331.

- Gringarten, A. and Sauty, J. (1975). A theoretical study of heat extraction from aquifers with uniform regional flow. *Journal of Geophysical Research*, 80(35):4956–4962.
- Gringarten, A. C. (1979). Reservoir lifetime and heat recovery factor in geothermal aquifers used for urban heating. In *Geothermics and Geothermal Energy*, pages 297–308. Springer.
- Hao, Y., Fu, P., and Carrigan, C. R. (2013). Application of a dual-continuum model for simulation of fluid flow and heat transfer in fractured geothermal reservoirs. In University, S., editor, *The 38th Stanford Geothermal Workshop*.
- Hill, R. (1963). Elastic properties of reinforced solids: some theoretical principles. *Journal of the Mechanics and Physics of Solids*, 11(5):357–372.
- Hyperworks, A. (2009). Hypermesh users manual.
- Kolditz, O., Bauer, S., Bilke, L., Böttcher, N., Delfs, J.-O., Fischer, T., Görke, U. J., Kalbacher, T., Kosakowski, G., McDermott, C., et al. (2012). Opegeosys: an open-source initiative for numerical simulation of thermo-hydro-mechanical/chemical (thm/c) processes in porous media. *Environmental Earth Sciences*, 67(2):589–599.
- Long, J., Remer, J., Wilson, C., and Witherspoon, P. (1982). Porous media equivalents for networks of discontinuous fractures. *Water Resources Research*, 18(3):645–658.
- Long, J. and Witherspoon, P. A. (1985). The relationship of the degree of interconnection to permeability in fracture networks. *Journal of Geophysical Research: Solid Earth*, 90(B4):3087–3098.
- McLarty, L. and Grabowski, P. (1998). Enhanced geothermal systems. Technical report, Princeton Economic Research, Inc., Rockville, MD (US).
- Neuman, S. P. (1988). Stochastic continuum representation of fractured rock permeability as an alternative to the REV and fracture network concepts. In *Groundwater Flow and Quality Modelling*, pages 331–362. Springer.
- Nicol, A., Walsh, J., Watterson, J., and Gillespie, P. (1996). Fault size distributions - are they really power-law? *Journal of Structural Geology*, 18(2):191–197.
- Pearson, K. (1894). Contributions to the mathematical theory of evolution. *Philosophical Transactions of the Royal Society of London. A*, 185:71–110.
- Reches, Z. (1986). Networks of shear faults in the field and in experiments. In *Fragmentation, form and flow in fractured media*, volume 8, pages 42–51. Israel Physics Society.
- Robertson, E. C. (1988). Thermal properties of rocks. Technical report, United States Geological Survey.
- Sahimi, M. (2011). *Flow and transport in porous media and fractured rock: from classical methods to modern approaches*. John Wiley & Sons.
- Sambridge, M. and Mosegaard, K. (2002). Monte carlo methods in geophysical inverse problems. *Reviews of Geophysics*, 40(3).

- Satman, A. (2011). Sustainability of geothermal doublets. In *Proceedings, Thirty-Sixth Workshop on Geothermal Reservoir Engineering, Stanford University, Stanford, California, U.S.A.*
- Schwartz, F. W. and Smith, L. (1988). A continuum approach for modeling mass transport in fractured media. *Water Resources Research*, 24(8):1360–1372.
- Si, H. (2007). Tetgen. *Numerical Mathematics and Scientific Computing, Weierstrass Institute for Applied Analysis and Stochastics (WIAS), Berlin, Germany, tetgen. berlios. de.*
- Willis, M. E., Burns, D. R., Rao, R., Minsley, B., Toksöz, M. N., and Vetri, L. (2006). Spatial orientation and distribution of reservoir fractures from scattered seismic energy. *Geophysics*, 71(5):O43–O51.
- Witherspoon, P. A., Wang, J. S., Iwai, K., and Gale, J. E. (1980). Validity of cubic law for fluid flow in a deformable rock fracture. *Water Resources Research*, 16(6):1016–1024.

Appendix A

Supplementary Images and Plots

A-1 Pumping Rate Test

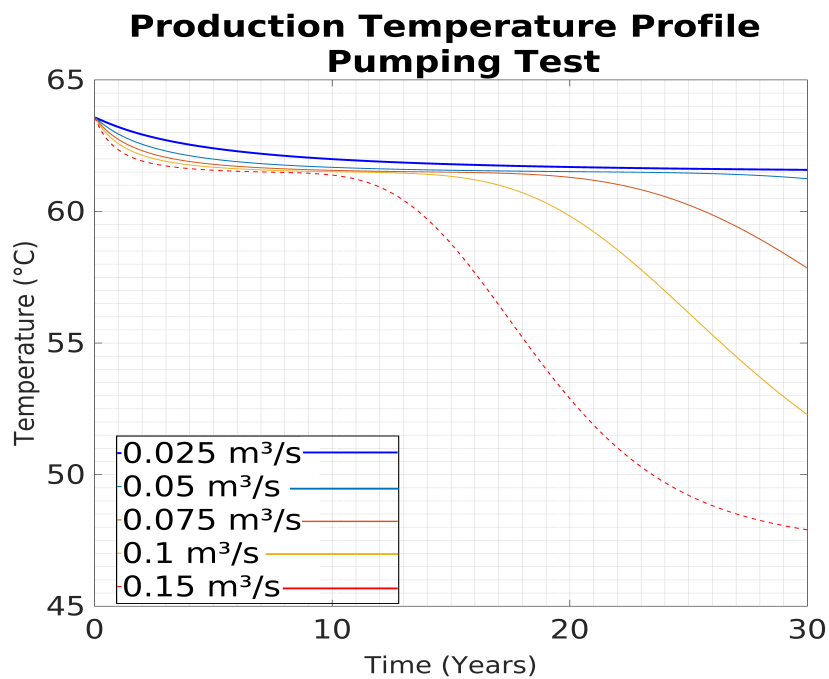


Figure A-1: Temperature production profile for varying pumping rates while holding all other parameters constant. Increased pumping rate corresponding to increased temperature drawdown and earlier thermal breakthrough

A-2 Azimuth Study

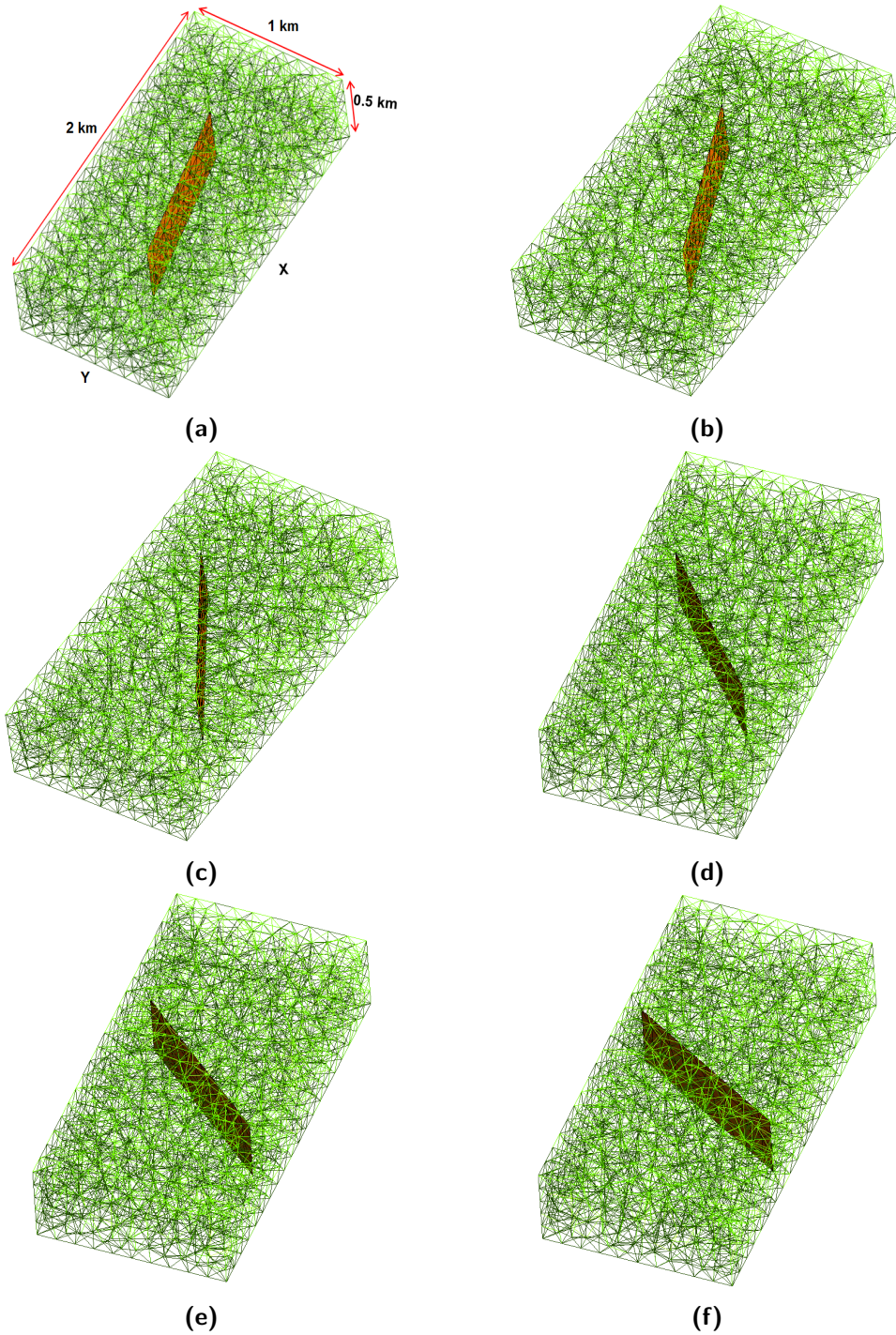


Figure A-2: Meshes used for Azimuth study: (a)10° (b)20° (c)30° (d)40° (e)50° (f)60°

A-3 Single Fracture Permeability Experiment - Geometry II

A-3-1 Low Permeability

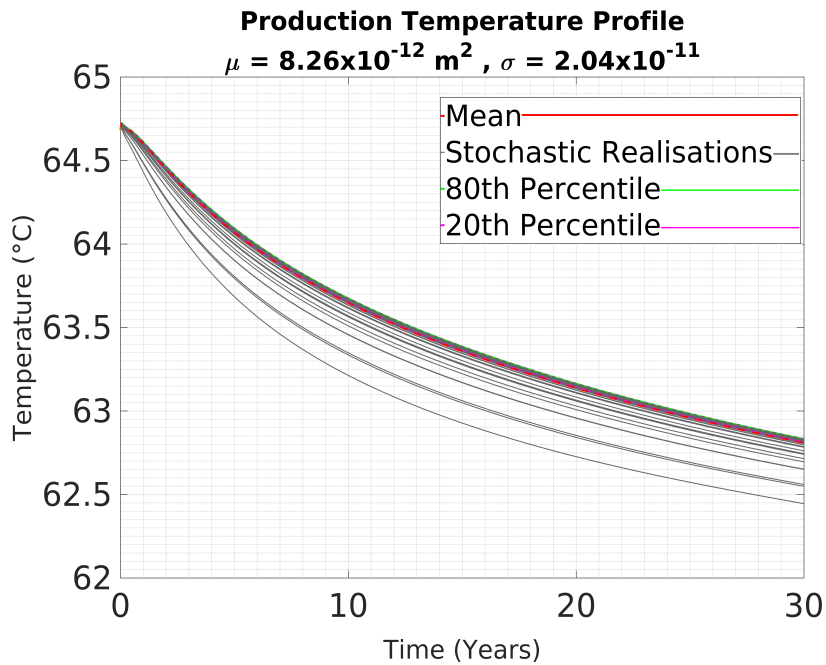


Figure A-3: Production Temperature Profile for high permeability single fracture embedded in geometry II

Time (years)	5	10	15	20	25	30
Average Temp.	64.07	63.65	63.36	63.14	62.96	62.81
Mode	63.69	63.21	62.93	62.73	62.57	62.45
Standard Deviation	0.07	0.07	0.07	0.07	0.07	0.06
80th Quantile	64.10	63.68	63.39	63.17	62.99	62.83
20th Quantile	64.08	63.65	63.36	63.14	62.96	62.81
Skewness	5.84	5.82	5.83	5.82	5.81	5.84

Table A-1: Summary of statistics for single fracture embedded in geometry II with low

A-3-2 High Permeability

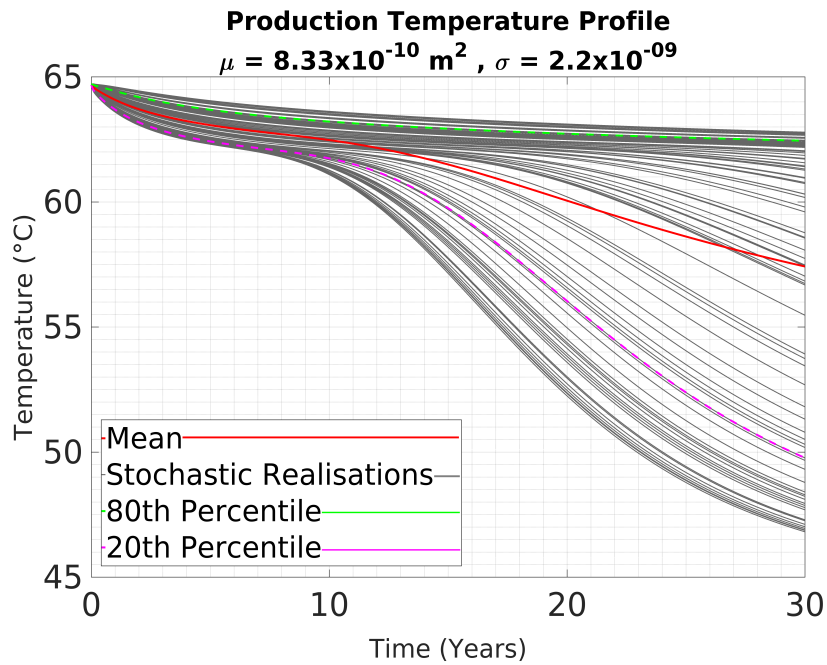


Figure A-4: Production Temperature Profile for high permeability single fracture embedded in geometry II

Time (years)	5	10	15	20	25	30
Average Temp.	63.07	62.47	61.50	60.05	58.62	57.42
Mode	62.30	61.09	57.14	52.24	48.78	46.81
Standard Deviation	0.58	0.74	1.83	3.56	4.98	5.87
80th Quantile	63.68	63.21	62.93	62.73	62.57	62.44
20th Quantile	62.42	61.74	59.75	56.04	52.38	49.77
Skewness	1.32	1.87	2.38	2.19	1.97	1.81

Table A-2: Summary of statistics for single high permeability fracture embedded in geometry II

Appendix B

Data Files and Formats

B-1 OpenGeoSys File Format

Table B-1: Required Input Files

File Extension	Description
GLI	Geometric Object definition
BC	Dirichlet Boundary Conditions
IC	Initial Conditions
ST	Source Term
MFP	Fluid Phase Properties
MSP	Solid Phase Properties
MMP	Medium Properties (Matrix + Fractures)
NUM	Numerical settings
TIM	Time stepping control
OUT	Result output settings
PCS	Physical process definition
MSH	Finite Element Mesh

B-1-1 Input File Examples

Geometry File - .gli

```
#POINTS 1
0 0 0 0
1 2000 0 0
2 2000 1000 0
3 0 1000 0
4 0 0 -500 6
5 2000 0 -500
6 2000 1000 -500
7 0 1000 -500
8 500 500 -400 $NAME Inj 11
9 1500 500 -400 $NAME Pro2000
```

```

10 2000 1500 -400 $NAME Monitor
#POLYLINE
$ID
1
$NAME
Top
$TYPE
2
$EPSILON
1e-4
$MAT_GROUP
-1
$POINTS
0
1
2
3
0
#POLYLINE
$ID
2
$NAME
Base
$TYPE
2
$EPSILON
1e-4
$MAT_GROUP
-1
$POINTS
4
5
6
7
4
#SURFACE
$ID
0
$NAME
Top
$TYPE
0
$EPSILON
0.1
$MAT_GROUP
-1
$POLYLINES
Top
#SURFACE
$ID
1
$NAME
Base
$TYPE
0
$EPSILON
0.1
$MAT_GROUP
-1
$POLYLINES
Base
#STOP

```

Boundary Condition File - .bc

The boundary conditions can be defined on geometrical features which must be defined in the .gli file. The default condition for bounding surfaces in OpenGeoSys is no-flow or no-flux so no additional BC needed to be defined as the default case fit the assumptions in this study. The BC file was used to set the temperature of the water being injected into the reservoir at a constant value of 313.15 K.

```

GINA - Boundary Condition
#BOUNDARY_CONDITION
$PCS_TYPE
HEAT_TRANSPORT
$PRIMARY_VARIABLE
TEMPERATURE1
$GEO_TYPE
POINT Inj
$EPSILON
1e-4
$DIS_TYPE
CONSTANT 313.15
#STOP

```

Initial Condition File- .ic

```

#INITIAL_CONDITION
$PCS_TYPE
LIQUID_FLOW
$PRIMARY_VARIABLE
PRESSURE1
$GEO_TYPE
DOMAIN
$DIS_TYPE
GRADIENT 0 14715000 9.81e+3 ; 1.5 km depth to top res
#INITIAL_CONDITION
$PCS_TYPE
HEAT_TRANSPORT
$PRIMARY_VARIABLE
TEMPERATURE1
$GEO_TYPE
DOMAIN
$DIS_TYPE
GRADIENT 0 328.95 0.0222
#STOP

```

Source Term File - .st

```

GeoSys-ST: Source Terms -----
#SOURCE_TERM
$PCS_TYPE
LIQUID_FLOW
$PRIMARY_VARIABLE
PRESSURE1
$GEO_TYPE
POINT Inj
$DIS_TYPE
CONSTANT_NEUMANN 0.05
#SOURCE_TERM
$PCS_TYPE
LIQUID_FLOW
$PRIMARY_VARIABLE
PRESSURE1
$GEO_TYPE
POINT Pro2000
$DIS_TYPE
CONSTANT_NEUMANN -0.05
#STOP

```

Fluid Properties File - .mfp

```

GeoSys-MFP: Material Fluid Properties -----
#FLUID_PROPERTIES
$FLUID_TYPE
LIQUID
$DAT_TYPE
LIQUID
$DENSITY
1 983
$VISCOSITY
1 4.6e-4
$SPECIFIC_HEAT_CAPACITY
1 4186
$HEAT_CONDUCTIVITY
1 0.6
#STOP

```

Solid Properties File - .msp

```

Gina - MSP-Datei
#SOLID_PROPERTIES
$DENSITY
1 2763
$THERMAL
EXPANSION
2.4e-5
CAPACITY
1 908
CONDUCTIVITY
1 3.35
#SOLID_PROPERTIES
$DENSITY
1 2763
$THERMAL
EXPANSION
2.4e-5

```

```

CAPACITY
1 908
CONDUCTIVITY
1 3.35
#STOP
Volumetric Thermal Expansion based on Limestone

```

Medium Properties File - .mmp

This file is used to define properties of the two media which exist in the reservoir, the fracture and rock matrix. The file is connected to the mesh file, in that two blocks of parameters which begin with the identifier #MEDIUM_PROPERTIES must be written to correspond with the order of the material numbers in the mesh file. So the first block of parameters are applied to the material number 0 and the second to material number 1 in this case.

```

GeoSys-MMP: Material Medium Properties -----
#MEDIUM_PROPERTIES
$GEOMETRY_DIMENSION
2
$GEOMETRY_AREA
0.0001
$POROSITY
1 1.0
$TORTUOSITY
1 1.000000e+000
$STORAGE
1 1.0e-10
$PERMEABILITY_TENSOR
ISOTROPIC 8.33e-10
$DENSITY
1 983
$HEAT_DISPERSION
0 0 0 ; longitudinal transverse in W/m2 K
#MEDIUM_PROPERTIES ;matrix
$GEOMETRY_DIMENSION
3
$GEOMETRY_AREA
1
$POROSITY
1 0.014
$TORTUOSITY
1 1.000000e+000
$STORAGE
1 1.0e-10
$PERMEABILITY_TENSOR
ISOTROPIC 9.9e-18
$DENSITY
1 983
$HEAT_DISPERSION
0 0 0 ; longitudinal transverse in W/m2 K
#STOP

```

Numerical Settings Parameter File - .num

```

$OVERALL_COUPLING
:min_iter -- max_iter
1 1
#NUMERICS
$PCS_TYPE
LIQUID_FLOW
$LINEAR_SOLVER
; method error_tolerance max_iterations theta precondition storage
2 6 1.0e-11 3000 1.0 1 2
$NON_LINEAR_ITERATIONS
; method error_tolerance max_iterations relaxation tolerance
PICARD LMAX 100 0 1e-3
$COUPLING_CONTROL
;error method -- tolerances
LMAX 1.e-3
#NUMERICS
$PCS_TYPE
HEAT_TRANSPORT
$LINEAR_SOLVER
; method error_tolerance max_iterations theta precondition storage
2 6 1.0e-011 3000 1 1 4
$NON_LINEAR_ITERATIONS
; method error_tolerance max_iterations relaxation tolerance

```

```

    PICARD LMAX 100 0 1e-3
$COUPLING_CONTROL
:error method -- tolerances
LMAX 1.e-3
$ELE_MASS_LUMPING 28
1
$ELE_SUPG
1 0 0
#STOP

```

Time Stepping File - .tim

```

#TIME_STEPPING
$PCS_TYPE
LIQUID_FLOW 3
$TIME_START
0.0
$TIME_END
946080000 ; 30Jahre
$TIME_STEPS 8
1500 630720
#TIME_STEPPING
$PCS_TYPE
HEAT_TRANSPORT
$TIME_START 13
0.0
$TIME_END
946080000 ; 30Jahre
$TIME_STEPS 18
1500 630720
#STOP

```

Output Settings File - .out

```

#OUTPUT 1
$PCS_TYPE
LIQUID_FLOW
$NOD_VALUES
PRESSURE1
TEMPERATURE1 6
$ELE_VALUES
VELOCITY1_X
VELOCITY1_Y
VELOCITY1_Z
$GEO_TYPE 11
DOMAIN
$DAT_TYPE
VTK
$TIM_TYPE
STEPS 150 ; every 3rd year 16
#OUTPUT
$PCS_TYPE
HEAT_TRANSPORT
$NOD_VALUES
TEMPERATURE1 21
$GEO_TYPE
POINT Pro2000
$DAT_TYPE
TECPLOT
$TIM_TYPE 26
STEPS 1
#STOP

```

Process Settings File - .pcs

```

#PROCESS
$PCS_TYPE
LIQUID_FLOW
$PRIMARY_VARIABLE
PRESSURE1
$TIM_TYPE
TRANSIENT 4
#PROCESS
$PCS_TYPE 9
HEAT_TRANSPORT
$PRIMARY_VARIABLE
TEMPERATURE1
$TIM_TYPE
TRANSIENT 14
#STOP

```

B-2 GMSH Files

```

Point(1) = {0, 0, 0, 100}; //Defining points
Point(2) = {4000, 0, 0, 100};
Point(3) = {4000, 3000, 0, 100};
...
...
Point(10) = {1000, 1500, -450, 100};
Point(11) = {3000, 1500, -450, 100};
Point(12) = {3000, 1500, -50, 100};
Line(1) = {1, 2}; //Defining lines
Line(2) = {2, 3};
Line(3) = {3, 4};
...
...
Line(14) = {10, 11};
Line(15) = {11, 12};
Line(16) = {12, 9};
Line Loop(18) = {5, 6, 7, 8};
Plane Surface(18) = {18}; //Defining Surfaces
Line Loop(20) = {1, 2, 3, 4};
Plane Surface(20) = {20};
Line Loop(22) = {13, 14, 15, 16};
Plane Surface(22) = {22};
Line Loop(24) = {4, 9, -8, -12};
Plane Surface(24) = {24};
Line Loop(26) = {3, 12, -7, -11};
Plane Surface(26) = {26};
Line Loop(28) = {2, 11, -6, -10};
Plane Surface(28) = {28};
Line Loop(30) = {1, 10, -5, -9};
Plane Surface(30) = {30};
Surface Loop(34) = {20, 30, 28, 26, 24, 18}; //Defining Volume
Volume(34) = {34};
Physical Surface(0) = {22}; //Set material number for fracture(2D) elements
Physical Volume(1) = {34}; //Set material number for matrix(3D)elements
Surface{22} In Volume{34}; //Command shared nodes between 2D and 3D mesh elements

```

Appendix C

Programming

C-1 Python

C-1-1 Python: Conversion of Petrel DFN for HyperMesh

```
# -*- coding: utf-8 -*-
"""
Created on Sun Apr 10 15:29:34 2016

@author: Ariel Thomas
"""
#=====
# The following code can be used to convert a discrete fracture model (DFN)
# generated by Petrel (FAB) to a file format that can be read by HyperMesh (.tcl) for
# FE mesh generation. Please note the following before utilizing this code:
# 1. The program assumes that all the fractures are 4 sides,
#    characterized by 4 corner points (this can be specified
#    in Petrel DFN module)
# 2. It is assumed that the model geometry is simple block representation
#    of a reservoir unit defined by 8 geometrical corner points and 12 lines
#    connecting them (i.e top, base and 4 sides) N.B. This is 'hardwired' into
#    the code.
# 3. The reservoir geometry point data should be saved in a file named 'output.tcl'.
#    This file should contain the 8 points which define the corners of the model.
# 4. The corresponding line data should be stored in a separate text file named
#    'lines.tcl'
# 5. The program should be run cell by cell and the output text files temp1-3
#    should be checked for QC to ensure everything went smoothly.
# 6. All header and footer information should be removed from the fracture attribute
#    file generated by Petrel. Be careful!! there are 5 or 6 lines of text at the
#    end of the FAB file.

#                               Happy Meshing :)
#=====
pet = open('VF13.txt','r') # input the name of the Petrel file with all headers removed
att = open('attr_VF13.txt','w')
orig=pet.name

#place fracture attributes into a new file
for line in pet.readlines():
    if len(line.split()) > 4 :
        att.write(line)
att.close()
pet.close()
att =open('attr_VF13.txt','r')
frac_cnt =len(att.readlines())
pt_cnt =4*frac_cnt # determines the number of points : 4*(no of frags).
```

```

att.close() 50

### Remove lines with Petrel specific data
pet = open(orig, 'r')
temp1 = open('temp1.txt', 'w')
for line in pet.readlines(): 55
    if line[4]!="0":
        temp1.write(line)

temp1.close()
pet.close() 60
### Remove lines with attributes
#####
# The FAB file generated by Petrel contains lines with the fracture number,
# aperture, permeability and other values which characterize the fracture set
# inside the Petrel environment.
##### 65
temp1 = open('temp1.txt', 'r')
temp2 = open('temp2.txt', 'w')

for line in temp1.readlines(): 70
    if len(line.split()) == 4 :
        temp2.write(line) #this file contains only x,y,z locations
temp1.close()
temp2.close() 75

### Remove redundant points
#####
# Petrel generates most fractures with 4 points but sometimes
# they contain 5 points which is not necessary for simulation as all
# fractures are assumed to have 4 sides.
##### 80
pts = open('temp2.txt', 'r')
pts3 = open('temp3.txt', 'w')

for line in pts.readlines(): 85
    if line[4]!="5":
        pts3.write(line)

pts.close() 90
pts3.close()

### Appending fracture geometry point data to the .geo file
f = open('temp3.txt', 'r')
out = open('output.tcl', 'a') 95
cnt = 8 # assumes that 8 points already exist in the .geo file
a=1
while a < pt_cnt:
    for line in f.readlines(): 100
        coords = line.split()
        x= coords[1]
        y= coords[2]
        z= coords[3]
        out.write(" *createnode %s %s %s 0 0 0 \n" % (x,y,z))
    a+=1 105
out.close()
### Appends the line data to the end of the file that now contains all
# the point data corresponding to the fractures imported from Petrel
f = open('lines.tcl', 'r')
out = open('output.tcl', 'a') 110
out.write("\n\n #Top and Base Lines \n\n")
for line in f.readlines():
    out.write(line)
f.close()
out.close() 115
### Appending Lines

f = open('output.tcl', 'a')
i=13
cnt=1 120
f.write("\n\n #Fracture Lines \n\n")
for cnt in range(pt_cnt):
    if i % 4 !=0:
        f.write(" *createlist nodes 1 %d %d \n" 125
                " *linecreatefromnodes 1 0 150 5 179\n" % (i-4,i-3))
    else:
        f.write(" *createlist nodes 1 %d %d \n"
                " *linecreatefromnodes 1 0 150 5 179\n" % (i-4,i-7))
    i+=1
f.close() 130
### Appending surfaces for fractures ( NB Model boundaries are not included here)
f = open('output.tcl', 'a')
# 8 lines account for the model boundaries and +1 to start at the next number in the sequences of
elements
li=9
f.write("\n\n #Fracture Surface: NB Mesh First!! \n\n") 135

for cnt in range(frac_cnt):
    f.write(" *createmark lines 1 %d %d %d %d \n"

```

```

                "createplane 1 1 0 0 0 0\n"
                "splinesurface lines 1 1 1 1 \n" %(li,li+1,li+2,li+3))
    li+=4
f.close()

f = open('surfs.tcl','r')
out = open('output.tcl','a')
out.write("\n \n #Top and Base Surface : Create volume! \n")

for line in f.readlines():
    out.write(line)
f.close()
out.close()

```

C-1-2 Python: Generating multiple input files

```

# -*- coding: utf-8 -*-
"""
Created on Mon Jun 6 14:46:03 2016

@author: athomas
"""
import subprocess
f=open('make_new_inputs.sh','w')
f.write('#!/bin/bash \n'
        'clear \n'
        'echo "The script begins now..." \n')
res = 10 #defines the simulation number
x = 1
# Following loop generates a shell script which copies the input files
# from a template set of input files.
for i in range(100): # range defines the number of realisations to be generated
    f.write('cp res%d.gli res%d_%d.gli \n'
            'cp res%d.msh res%d_%d.msh \n'
            'cp res%d.tim res%d_%d.tim \n'
            'cp res4edit.out res%d_%d.out \n'
            'cp res%d.num res%d_%d.num \n'
            'cp res%d.pcs res%d_%d.pcs \n'
            'cp res%d.mfp res%d_%d.mfp \n'
            'cp res%d.msp res%d_%d.msp \n'
            'cp res%d.mmp res%d_%d.mmp \n'
            'cp res%d.ic res%d_%d.ic \n'
            'cp res%d.st res%d_%d.st \n'
            'cp res%d.bc res%d_%d.bc \n'
            'cp res%d.sh res%d_%d.sh \n'
            'echo "Moving to next file..." \n'
            'echo \n')
    %(res, res, x, res, res, x, res, res, x, res, x, res, res, x, res, res, x, res, res, x, res, res, x,
      res, res, x, res, res, x, res, res, x)
    x+=1

f.write('echo "Files Copied" \n'
        ', -')
f.close()

subprocess.call(['./make_new_inputs.sh']) #Runs the shell script

f.close()

### GENERATE MULTIPLE MMP Files
fn = open('permvals_med.txt','r') #opens text file with parameters generated by Matlab
fo = open('appvals_med.txt','r')
perm = fn.readlines()
app = fo.readlines()
l=20
# INPUT MODEL NUMBER HERE
for i in range(100):
    f = open('res%d_%d.mmp' %(res, i+1), 'w')
    f.write('#MEDIUM_PROPERTIES \n'
            '$GEOMETRY_DIMENSION \n'
            '2 \n'
            '$GEOMETRY_AREA \n'
            '%s \n'
            '$POROSITY \n'
            '1 1.0 \n'
            '$TORTUOSITY \n'
            '1 1.000000e+000 \n'
            '$STORAGE \n'
            '1 1.0e-10 \n'
            '$PERMEABILITY_TENSOR \n'
            'ISOTROPIC %s \n'
            '$DENSITY \n'
            '1 983 \n'
            '$HEAT_DISPERSION \n'
            '0 0 0 ; longitudinal transverse in W/m2 K \n'
            '#MEDIUM_PROPERTIES ;matrix \n'
            '$GEOMETRY_DIMENSION \n')

```

```

        ' 3\n'
        '$GEOMETRY_AREA\n'
        ' 1\n'
        '$POROSITY\n'
        ' 1 0.014\n'
        '$TORTUOSITY\n'
        ' 1 1.00000e+000\n'
        '$STORAGE\n'
        ' 1 1.0e-10 \n'
        '$PERMEABILITY_TENSOR\n'
        ' ISOTROPIC 9.9e-18\n'
        '$DENSITY\n'
        ' 1 983\n'
        '$HEAT_DISPERSION\n'
        ' 0 0 0 ; longitudinal transverse in W/m2 K\n'
        '#STOP' %(app[i],perm[i])) # inserts the random values into the .mmp file
f.close()
fn.close()
%%% Generate Job Scripts

for i in range(100):
    f= open('res%d_%i.sh' %(res,i+1),'w')
    f.write('#BSUB -J RES%d_%i \n'
           '#BSUB -n 8 \n'
           '#BSUB -a openmp \n'
           '#BSUB -W 1:30\n'
           '#BSUB -M 1000\n'
           '#BSUB -u ariel.t.thomas@gmail.com\n'
           '#BSUB -B\n'
           '#BSUB -N\n'
           '#BSUB -P gge\n'
           '\n'
           'ogs res%d_%i\n' %(res,i+1,res,i+1))
f.close()

```

C-2 Matlab

C-2-1 Matlab: Generation of random fracture parameters

```

% Generating probability distribution of Fracture parameters
% Author : Ariel Thomas
% Description : This script generates a probability distribution based on
% user defined mean and standard deviation. A pre-defined number of values
% are then randomly drawn from this distribution and written to a text file
%% Log Normal Distribution of Aperture-----
%Defining parameters of the log normal distribution mu and sigma
m = 8.33e-10;
sigma = 1.1;
v = m^2*exp(sigma^2)-m^2;
mu = log((m^2)/sqrt(v+m^2));
r = lognrnd(mu,sigma,200,1); %generating the random values
aperture = sqrt(r.*12) %calculating the corresponding aperture
dlmwrite('permvals.txt',r,'\t');
dlmwrite('appvals.txt',aperture,'\t');

% Plotting Aperture PDF

figure
X= 0:m/1000:3*m;
Y=lognpdf(X,mu,sigma);
y_norm = zeros(length(Y));
y_norm = (Y(1,1:end)-Y(1))./max(Y);
area(X,y_norm)
xlabel(['\fontsize{18}Permeability (m^2)'])
ylabel(['\fontsize{18}Probability Density'])
title(['\fontsize{24}PDF of Fracture Permeability:' '\mu = 8.33x10^{-10} m^2 , \sigma=2.2x10^{-09}'
])

%%----- Normal Distribution of Azimuth-----
arg =30; %
azi = makedist('Normal','mu',arg,'sigma',5);

azimuth = random(azi,200,1);

dlmwrite('azivals.txt',azimuth,'\t');
figure
X_azi= 0:1:2*arg;
Y_azi=pdf(azi,X_azi);
area(X_azi,Y_azi,'LineWidth',2)
xlabel(['\fontsize{18}Azimuth (Deg)'])
ylabel(['\fontsize{18}Probability Density'])
title(['\fontsize{22}PDF of Fracture Azimuth:' '\mu = 30\circ , \sigma = 5'])

```

C-2-2 Matlab: Generation of Histogram Plots

```

%% Plotting Histogram of Experiment Results
1

%Creating vector of x axis values based on range of data
x5_pdf = [60:0.1:65]; %5 years
x15_pdf = [55:0.1:68]; %15 years
x30_pdf = [40:0.1:68]; %30 years
6
%generating histograms
[N5,e] = histcounts(res4_pro_five,25);
distfit_aphigh_5 = fitdist(res4_pro_five,'Normal')
m5 = mean(distfit_aphigh_5); % mean of the distribution
v5 = std(distfit_aphigh_5); % std deviation
y_five = pdf(distfit_aphigh_5,x5_pdf);
11

distfit_aphigh_15 = fitdist(res4_pro_fifteen,'Normal')
m15 = mean(distfit_aphigh_15); % mean of the distribution
v15 = std(distfit_aphigh_15); % std deviation
y_fifteen = pdf(distfit_aphigh_15,x15_pdf);
[N15,e] = histcounts(res4_pro_fifteen,25);
16

distfit_aphigh_30 = fitdist(res4_pro_thirty,'Normal')
m30 = mean(distfit_aphigh_30); % mean of the distribution
v30 = std(distfit_aphigh_30); % std deviation
y_thirty = pdf(distfit_aphigh_30,x30_pdf);
[N30,e] = histcounts(res4_pro_thirty,25);
21

26
figure
histogram(res4_pro_five,25)
hold on
sc = max(N5)/max(y_five);
x5 = ones(1,length(y_five)).*m5; % generating vector for plotting mean value
pdf5 = plot(x5,(y_five.*sc),'r','LineWidth',3)
xlabel({'\fontsize{26}Temperature ({\circ}C)'})
ylabel({'\fontsize{26}Bin Count'})
title({'\fontsize{26}Distribution of Production Temperature' ; 'N = 25, Time = 5 years'})
ax=gca;
ax.FontSize=16;
legend([pdf5],sprintf('Mean = %0.1f, Std. Dev. = %0.2f',m5,v5))
31

36
hold off
41

figure
histogram(res4_pro_fifteen,25)
hold on
sc2 = max(N15)/max(y_fifteen);
x15 = ones(1,length(y_fifteen)).*m15; % generating vector for plotting mean value
pdf15 = plot(x15,(y_fifteen.*sc2),'r','LineWidth',3)
xlabel({'\fontsize{26}Temperature ({\circ}C)'})
ylabel({'\fontsize{26}Bin Count'})
title({'\fontsize{26}Distribution of Production Temperature' ; 'N = 25, Time = 15 years'})
ax=gca;
ax.FontSize=16;
legend([pdf15],sprintf('Mean = %0.1f, Std. Dev. = %0.2f',m15,v15))
46

51
hold off
56

figure
histogram(res4_pro_thirty,25)
hold on
sc3 = max(N30)/max(y_thirty)
x30= ones(1,length(y_thirty)).*m30; % generating vector for plotting mean value
pdf30 = plot(x30,(y_thirty.*sc3),'r','LineWidth',3)
xlabel({'\fontsize{26}Temperature ({\circ}C)'})
ylabel({'\fontsize{26}Bin Count'})
title({'\fontsize{26}Distribution of Production Temperature' ; 'N = 25, Time = 30 years'})
ax=gca;
ax.FontSize=16;
legend([pdf30],sprintf('Mean = %0.1f, Std. Dev. = %0.2f',m30,v30))
61

66

```

